

POLITECNICO DI TORINO

Master's Degree in Biomedical Engineering



Master's Degree Thesis

Study of a thermal model for cancer treatment with laser ablation

Development of a feedback system to optimize liver optical
and thermal parameters using an integrated temperature
monitoring technique

Supervisors

Prof. Guido Perrone

Prof. Gianni Coppa

Prof. Alberto Vallan

Candidate

Alessandra Balestrino

Academic Year 2020/2021

*to those who truly love
and accept me.*

Summary

The rising in importance of minimally invasive surgical techniques goes unfortunately side by side with the increasing number of cancer cases worldwide, especially in poor countries. The fact that not every healthcare system can guarantee proper cures to all the citizens underline the importance of research in finding always cheaper protocols. Laser ablation is a new frontier that could open access to curing cancer also for those that nowadays cannot afford other treatments for the high cost of hospitalization and therapies as well.

Cancer is a pathological condition where the proliferation of cells in organs and tissues modifies the normal functioning and structure; for this reason any typology of mini-invasive surgical treatment, either hyperthermal or hypothermal, has the aim of forcing cells' necrosis.

The purpose of this master thesis have been to develop a thermal model that could help recreating the temperature distribution of liver during ablation. Moreover, the confrontation of the model with the experimental measures made during *ex-vivo* ablation gave the chance to evaluate liver optical and thermal parameters of the liver. The future goal will be to build an integrated sensing system in the delivery probe that calibrates the power real-time during the ablation.

Nowadays temperature monitoring, hence the effect of the power applied on the tissue, is mostly done with thermal Magnetic Resonance, while the integrated sensing system abovementioned is made with an array of Fibre Bragg Gratings. The linear relationship between temperature and the characteristic parameter of the gratings, the Bragg wavelength, simplifies the evaluation of the temperature distribution in the target.

These sensors have been used in the thesis' experiments after a previous characterization of FBGs made with MicronOptics and termocouple in order to find the parameters to find the Bragg wavelength.

Two kinds of array have been used: an *ultradense* array with 20 distributed FBGs staggered with respect to the core and an array with 20 FBGs in axis with the core. The former has helped to sense temperatures close to the tip of the laser, especially for the points along the trajectory; the latter instead was used for sensing temperature orthogonally in respect to the laser.

The model was made using **MATLAB® PDE toolbox**: this tool gives the possibility to solve Partial Differential Equations in different fields such as the study of thermal conductivity. The liver was modelled as a 2D cylinder section considering the delivery fibre along the central axis. The toolbox divides the section in meshes and works solving the heat equation for each area. The heat source has been modelled as punctual and with a Gaussian behaviour radially and an exponential decay along the axis. The optical parameters taken in account are scattering and absorption; the thermal parameter is the conductivity.

Once obtained the temperature distribution it has been compared to the measurements took during ablation with an optimization algorithm, *fminsearch*, to find parameters of absorption, scattering and conductivity that fit better the real problem.

Table of Contents

List of Tables	VII
List of Figures	VIII
Acronyms	XIII
1 Introduction	1
I Theoretic Aspects	4
2 Minimally Invasive Thermal Treatments in Oncology	5
2.1 Cryoablation	6
2.2 Radiofrequency Ablation	7
2.3 High Intensity Focused Ultrasound Ablation (HIFU)	8
2.4 Laser Ablation	9
3 Laser, Optical Fibre and Interaction with Tissues	11
3.1 Theory of Laser	11
3.2 Laser Diode	12
3.3 Optical Fibre	13
3.4 Optical Parameters	14
3.5 Interaction between laser and biological tissue	16
4 Fibre Bragg Gratings (FBGs)	20
4.1 Manufacture	22
4.2 Classification	25
4.3 Optical Interrogator: MicronOptics	27

II	Experimental Trials	29
5	Characterization of FBG array Sensors	30
5.1	Set up and Measurements	31
5.2	Results and Conclusions	35
5.3	Evaluation of self-heating	41
5.3.1	Set Up and Measurement	41
6	Creation of a Thermal Model	48
6.1	MATLAB®PDE Toolbox	48
6.1.1	Description of the Toolbox	48
6.1.2	Heat Transfer Problem	50
6.2	Model Realization	51
6.2.1	Geometry and Thermal Conditions	52
6.2.2	Modelization of liver ablation	54
6.2.3	Results and Conclusions	56
7	<i>Ex-vivo</i> Liver Ablation	61
7.1	Set up and Measurments	61
7.2	Results and Conclusion	68
8	Optimization	76
8.1	Algorithm principles	76
8.2	Results	77
9	Conclusions	81
A	MATLAB Codes	84
A.1	Characterization	84
A.2	Thermal model code	91
	Bibliography	94

List of Tables

3.1	Effects of temperature on biological tissues. [23]	19
5.1	λ_0 and k_T values for each FBG. Straight.	36
5.2	λ_0 and k_T values for each FBG. HD	36
5.3	Maximum temperature variation during the descending thermal gradient and maximum relative temperature error for each FBG. Straight	39
5.4	Maximum temperature variation during the descending thermal gradient and maximum relative temperature error for each FBG. HD	39
5.5	Organization of the tests performed to evaluate the self-heating effect.	41
5.6	Maximum temperature deviation for the FBGs in air during self-heating evaluation.	46
5.7	Maximum temperature deviation for the FBGs in water during self-heating evaluation	47
7.1	Current used to set the laser and its equivalent power value.	67
8.1	Values of the parameters optimized.	78
8.2	Temperature variation between the calculated and the evaluated temperature during the trials at 0.5 W.	78
8.3	Temperature variation between the calculated and the evaluated temperature during the trials at 1 W.	78
8.4	Temperature variation between the calculated and the evaluated temperature during the trials at 1.5 W.	79
8.5	Temperature variation between the calculated and the evaluated temperature during the trials at 2 W.	79

List of Figures

1.1	Estimated Increase in Cancer Cases [1]	1
1.2	Incidence, mortality and prevalence of cancer around the globe. [1]	2
2.1	Minimally Invasive Thermal Treatments for Tumor Removal.	6
2.2	Mechanism of cryoablation. The needle is inserted in the targer inducing different effects on different tissue level depending on the distance.	7
2.3	Example of RadioTherapy: US used for the correct placement of the probe	8
2.4	Diagrammatic illustration of the principle of HIFU. High-intensity ultrasound waves are generated by a transducer outside the body and focussed onto a small region deep within tissue.	9
2.5	MRI-guided laser ablation in the brain. MR thermometry provides feedback about the treatment real time.	10
3.1	Laser configuration. The energy is supplied by an external source and the energy of the laser is increased thanks to the cavity. [15] . .	12
3.2	Configuration of an optical fibre with materials specifiéc. [16]	13
3.3	Propagation of light between the complex core-cladding thanks to the different refractive index. [ref_index]	13
3.4	Different signals propagation between single-mode and multi-mode fibre. [17]	14
3.5	Scheme of Raman Scattering [18]	16
3.6	Absorbance of tissues at different wavelength.[19]	17
3.7	"Medical laser interaction map." [21]	17
4.1	Operating Principle of Fibre Bragg Gratings	20
4.2	FBG structure Inside the Optical fibre	21
4.3	Spectrum Shift After an External Perturbation.	22
4.4	Semplified Scheme of the Interferometric Method	24
4.5	Set Up for point-by-point technique. [26]	24

4.6	Scheme of the Phase Mask Method to imprint gratings in a photo-sensitive optical fibre. The diffracted plus and minus first orders are maximized. [26]	24
4.7	Uniform Bragg Grating Illustration.	25
4.8	Chirped Bragg Grating Illustration.	25
4.9	Tilted Bragg Grating Illustration	26
4.10	"Refractive index profile in the core of, 1) a uniform positive-only FBG, 2) a Gaussian-apodized FBG, 3) a raised-cosine-apodized FBG with zero-dc change, and 4) a discrete phase shift FBG." [27]	26
4.11	Broadband source Interrogator. [28]	27
4.12	Tunable Laser. [28]	27
4.13	Micron Optics HYPERION.	28
5.1	Scheme of the straight array and a zoom	31
5.2	Scheme of the ultra dense array and a zoom	31
5.3	Software interface of thermocouple launcher.	32
5.4	Set up for the FBGs characterization. A) is the plate used in the heating process of the D) metal block. B) Termocouple and C) FBGs array stick to the block with insulating plate. C) is covered in glass capillaries.	33
5.5	Interface of the software ENLIGHT while the straight array was connected.	35
5.6	Interface of the software ENLIGHT while the ultradense array was connected.	35
5.7	Calibration line: in blue the interpolating line is presented, in magenta the recorded data. Straight array.	37
5.8	Zoom of the calibration line: the point recorded overpass the interpolating line. Straight array.	37
5.9	Calibration line: in blue the interpolating line is presented, in magenta the recorded data. Ultradense array.	38
5.10	Zoom of the calibration line: the point recorded overpass the interpolating line. Ultradense array.	38
5.11	Comparison between the trends of the temperature measured by the thermocouple and evaluated by the straight array.	40
5.12	Comparison between the trends of the temperature measured by the thermocouple and evaluated by the ultradense array.	40
5.13	Laser module used for evaluating the self-heating.	42
5.14	Self-heating evaluation in air. A) Glass capillary to reduce the effect of strain on the fibre containing the FBGs array. B) Delivery fibre for laser delivery. C) FBGs array	43

5.15	Self-heating evaluation in water: the array is completely immersed in water. The laser is applied from the outside.	44
5.16	LabView interface to manage laser features. Two ways of emitting are possible: continuous and pulsed.	45
6.1	Geometry used for the model. The origin is in the middle of the right edge and that is where the tip of the laser has been put. . . .	52
6.2	a) Mesh realized using the function <code>createMesh</code> . The maximum value of edge is 0.09mm. b) Zoom to have a better perception of the triangulation.	53
6.3	Power density distributions for the Gaussian model.	56
6.4	Power density distributions for the rectangular model.	56
6.5	Temperature distribution and trends for the rectangular window. Power set at 0.5 W.	57
6.6	Temperature distribution and trends for the Gaussian window. Power set at 0.5 W.	57
6.7	Temperature distributions and trends for the rectangular window. Power set at 1 W.	58
6.8	Temperature distribution and trends for the Gaussian window. Power set at 1 W.	58
6.9	Temperature distributions and trends for the rectangular window. Power set at 1.5 W.	59
6.10	Temperature distribution and trends for the Gaussian. Power set at 1.5 W.	59
6.11	Temperature distributions and trends for the rectangular window. Power set at 2 W.	60
6.12	Temperature distribution and trends for the Gaussian. Power set at 2 W.	60
7.1	Data interpolation: calibration of the diode.	62
7.2	Complete Laser Unit. The keypad is used to insert the password, the power, the timer. When pushed, the red button below the display send the information of starting the emission. There is an emergency stop, a safety key and LEDs that help understanding laser status. .	63
7.3	Simple scheme of how optical fibres have been placed on the lower liver slice.	64
7.4	Real setup used for the trials. After each value of power all the gratings were moved in order not to affect the next results.	65
7.5	Zoom of the setup with the caliber.	65
7.6	Display when the device is turned on.	66
7.7	Liver after 180 s ablation with power 1 W.	69

7.8	Liver after 180 s ablation with power 1.5 W. On the right there is the lower slice where the laser was lean on, on the right there is the upper slice where we can see the effect of ablation anyway.	69
7.9	Liver after 180 s ablation with power 2 W.	70
7.10	Temperature trend during ablation for Array 1. 7.3	70
7.11	Temperature trend during ablation for Array 2. 7.3	71
7.12	Temperature trend 5 s before and 5 s after ablation for Array 3. 7.3	72
7.13	Temperature trend 5 s before and 5 s after ablation respect to the position for Array 1. 7.3	73
7.14	Temperature trend 5 s before and 5 s after ablation respect to the position for Array 2.	74
7.15	Temperature trend 5 s before and 5 s after ablation respect to the position for Array 3. 7.3	75
8.1	Comparison of the trend of the measured temperature and the one evaluated using optimization parameters. In red there are the measured ones and in blue the evaluated.	80

Acronyms

CSD

Constructive Solid Geometry

CW

Continuous Wave

FBG

Fibre Bragg Grating

FIR

Far-infrared

HIFU

High Intensity Focused Ultrasound

LA

Laser Ablation

LWIR

Long-wavelength infrared

MIR

Mid-wavelength infrared

NA

Numerical Aperture

NIR

Near-infrared

OFS

Optical Fibre Sensors

PDE

Partial Differential Equation

PW

Pulsed Wave

RFA

RadioFrequency Ablation

SWIR

Short-wavelength infrared

US

Ultrasound

Chapter 1

Introduction

Nowadays cancer is still one of the leading cause of premature death in the World. As reported by World Health Organization (WHO), the number of cases increased from 10 to 19.3 million between 2000 to 2020. It has also been estimated by WHO that in the next two decades 29 million new cases will be diagnosed and deaths led to cancer will be 16.3 million. Since the incidence rate increases with the age, the evaluation has only considered the progressive increase in world population and in people's average age. [1]

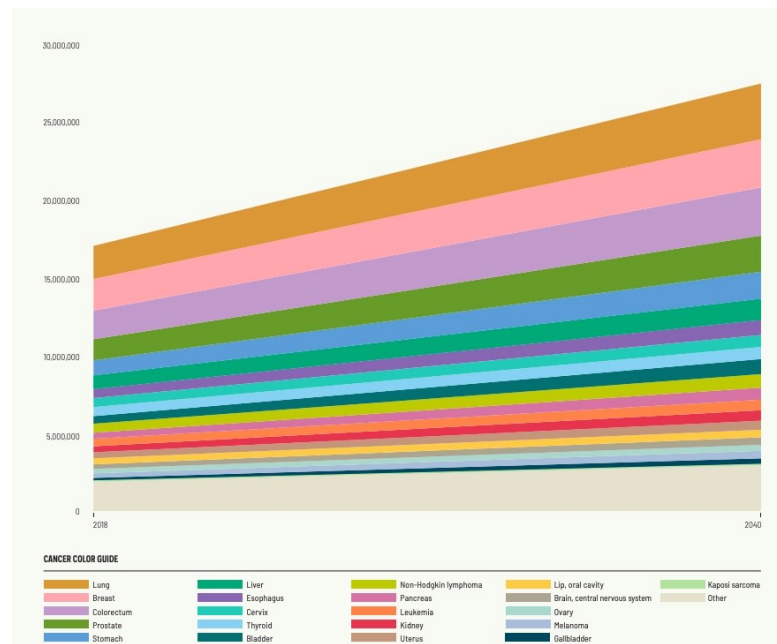


Figure 1.1: Estimated Increase in Cancer Cases [1]

Taking account of the risks factor would only worsen the already alarming bad scenario. Many of them could be prevented pursuing an healthy lifestyle: eating a balanced diet, practicing sports, avoid alcohol over-consumption and smoking - since this is the major cause for the developing of neoplasm. Not only cancer is a health problem, it is also an economical issue since the cost of treatments and health maintenance menace the economic growth of middle and poor country. [2] Primary and secondary prevention is almost cost-effective compared to the burden that cancer cures can represent for the economical system. Many countries has established programs where both prevention helps reducing mortality due to cancer.



Figure 1.2: Incidence, mortality and prevalence of cancer around the globe. [1]

Beside the increasing number of cases there is the demand of cancer surgery services: this aspect in particular underline the importance for science progress in order to accomplish society's right to health.

Usually surgery is applied in solid tumor contained in a specific area, though it's not granted for the patient not to need any more treatments after. Surgery in cancer cases is used to [3]:

- *Diagnose and stage a cancer;*
- *Removal of the entire cancerous area:* the whole cancerous tissue is removed using open surgery or laparoscopy;
- *Debulking:* the entire area cannot be removed because it would also damage healthy tissue, and so doctors proceed with a partial removal;
- *Palliative:* easing cancer symptoms removing a tumorous mass (not necessarily malignant) that applies a pressure on a nerve;

- *Restorative*: to return or change body's condition after surgery.

The most innovative technique is Laser Ablation (LA) for the preciseness and the possibility to reduce the exposition time. It is a thermal treatment that heats the target area with a light beam. All the therapies are in a specific wavelength range called *therapeutic window*: this is a compromise between the penetration depth - which is inversely proportional to the frequency of the wavelength - and the tissue absorption. Cells dies within few seconds because of protein denaturation that occurs around 50°C. Imaging techniques such as CT or MRI can support the treatment monitoring the temperature distribution, especially to reduce the damage of the healthy tissue that enclose the target area.

The challenge is to have an easier system to do such a complex analysis. Fibre Bragg Gratings (FBGs) could be the answer: these small sensors can be integrated in the optical fibre that delivers the therapy and help to have a better calibration and to adjust the power supplied real-time and have a better calibration.

Since there is not yet a definitive cure for cancer the importance of this study is not only bound to the science progress itself, but mostly to guarantee a better quality of life for as much people as possible.

"This much is clear: we simply must do better to ensure everyone can benefit from advances in the fight against cancer. [...] progress is not only possible, but also achievable." - Gary Reedy Chief Executive Officer, American Cancer Society.

Part I

Theoretic Aspects

Chapter 2

Minimally Invasive Thermal Treatments in Oncology

Surgery is the oldest approach in oncology. We can distinguish two types of surgery [3]

- *Neoadjuvant* : when surgery is done after other treatments.
- *Adjuvant*: when surgery is done before other treatments.

In both cases other therapies such as chemotherapy or radiotherapy are needed to cure the cancer. Although, after diagnosis, focal tumors are preferred to be treated with surgery.

Thanks to medical advances in technology, minimally invasive surgery has been possible and has offered an alternative to open surgery in terms of cost, recovery and reduction of after-surgery complications: also, operations can last longer, on the other hand hospitalization time is shorter. Moreover, from the aesthetic point of view, scars are way less visible. Between the range of different minimally invasive surgeries thermal ablation is peculiarly relevant. It can also be performed using open surgery, but the approach usually used for the application is percutaneous or non invasive. Thermal tumor ablation is an extension of what Hippocrates said:

“what what cannot be cured by iron can be cured by fire.” [4]

Thermal ablation is defined as *the destruction of tissue by extreme hypothermia or hiperthermia* [4]. Cellular necrosis is induced anytime the temperature goes below -40°C or above 60°C . Of course the time of exposal depends on the temperature used during the therapy [5].

Pennes' equation of heat transfer allows to study both cases.

$$\rho C_p \frac{\delta T}{\delta t} = k \nabla^2 T + Q_h + Q_m + Q_p \quad (2.1)$$

where ρ is the density of the tissue (kg/m^3), C_p is the specific heat capacity ($\text{J}/\text{kg} \cdot \text{K}$), T is the temperature (K), t is time (s), k is thermal conductivity ($\text{W}/\text{m} \cdot \text{K}$), Q_h , Q_m and Q_p are heat flux contributions, respectively from the ablation source, the metabolic heat flux, and blood perfusion.

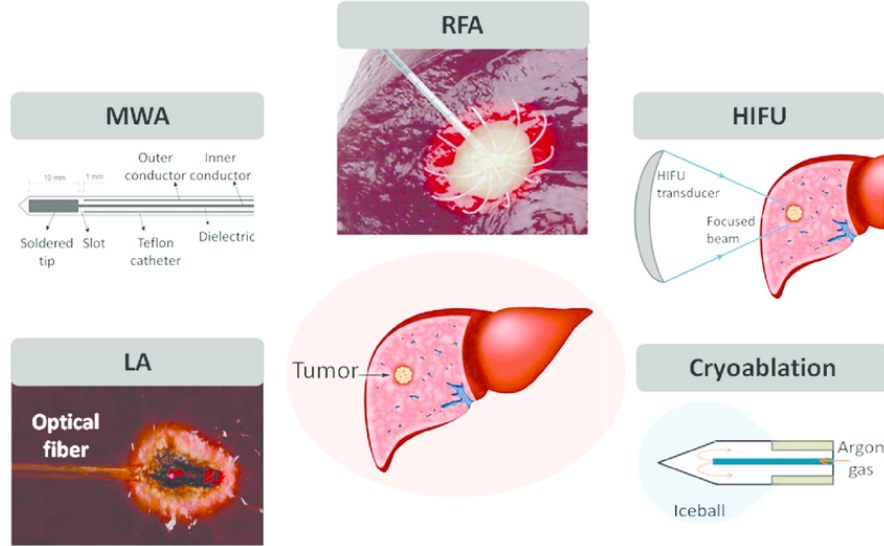


Figure 2.1: Minimally Invasive Thermal Treatments for Tumor Removal.

The goal in thermal ablation is obtained creating a wider gap between Q_h and Q_p - usually Q_m can be not taken into account since its changes are slower than the others. Most of the techniques that we will take in account can be both performed superficially or internally: in this case CT (computer tomography) and MRI (magnetic resonance imaging) are performed as well. First of all they are used to make the diagnose and choose the best therapy for the specific case; in case thermal ablation is chosen, either CT or MRI can be integrated during the surgery for the correct placement of the probe. Furthermore, MR thermal imaging helps to evaluate the temperature during the treatment and choose the correct feedback thermal dose; it also enhances the spatial control. [4]

2.1 Cryoablation

Cryoablation is a procedure where the flow of an extreme cold liquid - usually nitrogen, nitrous oxide - or a gas - such as compressed argon - thru a probe induces the destruction of the tissue: it is an energy deprivation strategy. Since there are many factors, including the type of cryoprobe used during the treatment, it is not simple to define a “*cryoablative dose*” [6].

Cells are damaged by the formation of ice crystals in the extracellular region that absorb water from the cells and shear forces begin to stress and affect cell's membrane integrity; as a response to the freeze concentration of solutes, the cell produces deleterious metabolic disturbances. Intracellular freezing occurs and is lethal: microcirculation fails and induces apoptosis and necrosis. The major part of cells already die at -40°C , but some cancer cells have shown a better resistance and needed a double freeze cycle. [7]

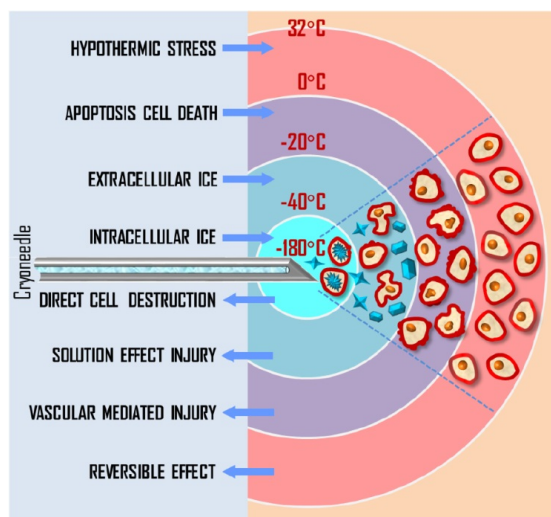


Figure 2.2: Mechanism of cryoablation. The needle is inserted in the target inducing different effects on different tissue level depending on the distance.

2.2 Radiofrequency Ablation

Radiofrequency ablation (RFA) is an extension of electrocautery and nowadays is the most diffused thermal ablative therapy. It is similar to an electrical circuit where the tissue is the resistive element. The current flow leads to ion agitation and heat generation thanks to *Joule Effect*. The interstitial electrode is placed in the target and a dispersive electrode is fixed to the skin surface. This set up is called *unipolar*. If two electrodes are applied to the tumor the configuration is called *bipolar*. The average volume treated goes from 1-3 cm up to 5 cm diameter. When the temperature of the tissue reaches 100°C dehydration occurs rapidly and make the impedance of the circuit spike and the power drops. This is the biggest limit of RF, but using single needle devices with internal water-cooling greater areas can be treated without the limitation of the heating itself.[8] Another solution is to use multi needle electrodes.

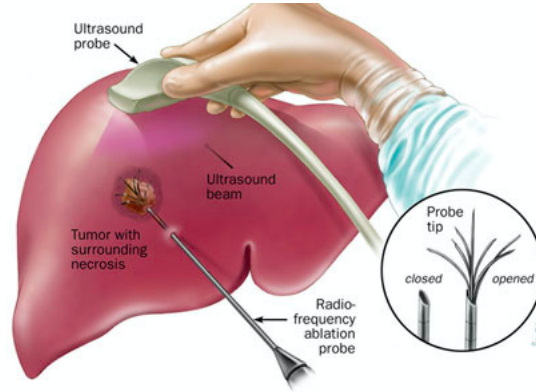


Figure 2.3: Example of RadioTherapy: US used for the correct placement of the probe

2.3 High Intensity Focused Ultrasound Ablation (HIFU)

High intensity focused ultrasound lately caught doctors' attention for the many advantages over other therapies, especially for the treatment of small localized tumor [9]. A single-focused US transducers supply the energy to the tissue while is moved percutaneously. An entire treatment is obtained overlapping several small focused areas, therefore it's a long-lasting therapy. The ultrasound wave across several tissues before reaching the target: transmission coefficient depends on the acoustic impedance Z .

The mechanical energy carried by the wave induces the heating of the tissue. The relationship between the intensity and the attenuation and scattering parameters is given by Lamber-Beer equation:

$$I = I_0 e^{-\mu x} \quad (2.2)$$

. For most tissue the attenuation coefficient α depends on the frequency

$$\mu_a = a f^b \quad (2.3)$$

where a and b are related to the tissue: the higher the frequency, the wider the attenuation. [10] HIFU transducers are excited sinusoidally at a frequency in the range of 0.5–8 MHz: an advantage of using this frequency range is that water attenuation is very low and the wave can reach the target with a sufficient energy. Usually higher frequencies are used for superficial tratments, while lower (in particular 0.5 MHz) to reach deep tissues.

Cells death is induced by necrosis within the focal volume, but the tissue in the propagation path is left unaffected [11].

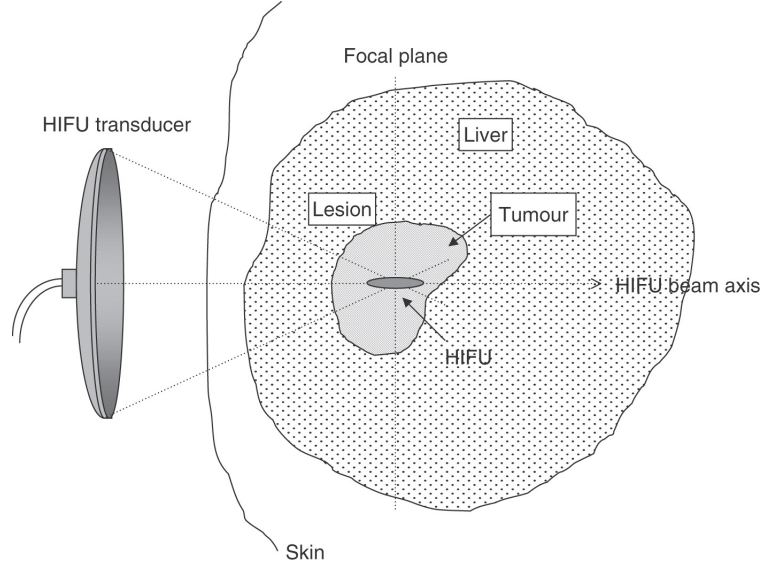


Figure 2.4: Diagrammatic illustration of the principle of HIFU. High-intensity ultrasound waves are generated by a transducer outside the body and focussed onto a small region deep within tissue.

[12]

2.4 Laser Ablation

In the past, laser has been used for other medical treatments than cancer ablation. The laser light is carried by a medium, usually a optical fiber with a diameter between 0.2 and 0.8 mm. Laser interacts with the tissue at three levels: absorption, scattering and reflection. The heating effect is obtained by absorption. [13] The optical response of the tissue is described by Beer-Lambert law:

$$E(z) = (1 - r)F_{sc}E_0e^{-\mu_{eff}z} \quad (2.4)$$

where $E(z)$ is the beam intensity attenuation in the tissue (W/m^2) at the depth z , E_0 is the incident irradiance (W/m^2), r is the Fresnel reflection coefficient for unpolarized light, F_{sc} is related to scattering, $\mu_{eff} = \mu_a + \mu_s$ is the effective absorption coefficient that considers both absorption and scattering at the used wavelength. As well as the former techniques, it induces thermal necrosis by heating; the final result is related to

- *Laser Settings*: it depends on the procedure. In continuous mode laser power range between 2 W to 30 W and the treatment time can last from few minutes to 20 minutes. In pulsed mode higher values of power (>100 W) are required to achieve the necrosis, but it requires a low duty-cycle and short time of emission;
- *Applicator characteristics*: this determines the geometry of the damage. It is very important to be able to restrain the power density and the temperature during the procedure. Nowadays new applicators have been designed with sapphire-tipped fibers to avoid the tip carbonization; furthermore a cooling system have been introduced;
- *Tissue optical and physical properties*: the amount and type of chromophores in the tissue also contribute to define the optical response of the tissue. These molecules are responsible for the absorption of light at a certain wavelength and also of the tissue response to the laser radiation. [14]

Laser light is highly energetic and as rapidly as it induces heating it is attenuated: in fact, the diameter of the ablations with a single laser applicator is usually below 2 cm. Multiple applicators may be a solutions for larger areas. In addition, MRI thermometry is used to control temperature distribution and help dosing power correctly. In this thesis, laser is the focus, in particular we have study an easier and more economic way for temperature monitoring and laser calibration in order to make LA (laser ablation) more commonly used to perform ablation, since now it requires highly expensive instrumentation.

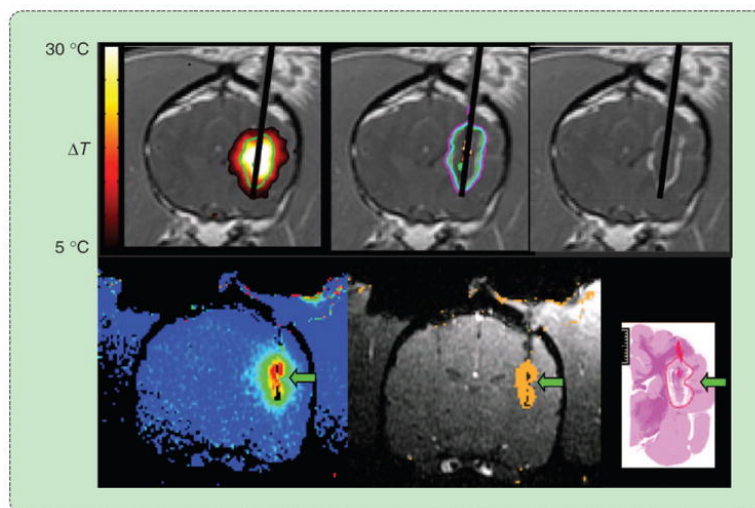


Figure 2.5: MRI-guided laser ablation in the brain. MR thermometry provides feedback about the treatment real time.

Chapter 3

Laser, Optical Fibre and Interaction with Tissues

Since lasers are used in our research here we are going to shortly analyze the physics of functioning. In addition, an overview of optical fiber is given for a better understanding of how the light is delivered to the tissue and how the tissue responds.

3.1 Theory of Laser

To understand lasers we should briefly introduce the concept of *simulated emission*. If an electron absorbs the energy of a photon at a certain wavelength it goes from a **grounded state** to an **excited state**. The electron can turn back to the resting state emitting a photon and this is called *spontaneous emission* and it occurs randomly. Although, if another photon at the right wavelength impacts the atom at his excited state it will return to the stable state emitting **two** simultaneous photons and this phenomenon is called *stimulated emission*: **population inversion** gives more chances to stimulated emission to occur. It requires a process called "pumping" that consists in the usage of an external energy source to increase the amount of atoms in the excited state and make more frequent the stimulated emission. Therefor, to build the simplest laser three elements are required: a pumping system, a gain medium and an optical cavity (Fig. 3.1). The gain medium is a material that can amplify light by stimulated emission; the pumping device supply energy to induce the population inversion. This energy can be an electric current or a light of a different wavelength. The gain medium is put in the optical cavity, which in the simplest configuration consists of two parallel mirror on the opposite sites of the medium. Lights is this way amplified since it bounces from side to side passing through the gain medium. The output coupler is partially reflective and

let stored photons to pass-by and form the laser. The medium can be gaseous, for example argon, liquid (organic dye) or solid (ruby, alexandrite) and diode. Peculiar properties of laser light are: **monochromaticity** -laser light contains just one wavelength or a very narrow band and this depends on the material, - **coherence** -for stimulated emission, radiation waves are in phase respect time and space- , and **collimation** - waves are parallel.

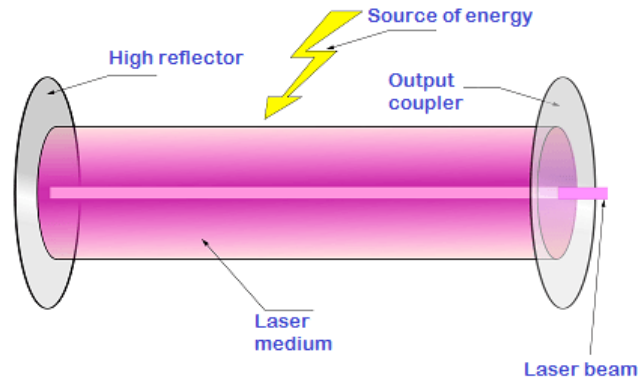


Figure 3.1: Laser configuration. The energy is supplied by an external source and the energy of the laser is increased thanks to the cavity. [15]

3.2 Laser Diode

A **laser diode** has been used in the laser unit for this Master Thesis work. The emission of laser light is on charged of the active region of the semiconductor material. The most common type is a p-n junction diode. The components are the following in order:

- **Metal contact;**
- **P-type conductor;**
- **Active region;**
- **N-type conductor;**
- **Metal contact**

The active region has the function of increasing the holes and electrons accumulate in the junction. In this way the power output is improved.

3.3 Optical Fibre

Laser light is guided by optical fibre, made by silica glass or plastic. From the inside out there is the internal **core** covered by the **cladding**: here is where light travels. External layers have only a protective function, thus are made by polymeric material to provide mechanical support and resistance. (3.2)

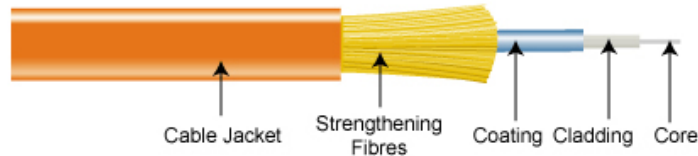


Figure 3.2: Configuration of an optical fibre with materials specified. [16]

The guided propagation takes place according to Snell's law, thanks to the variation of the refractive property of the glass. The glass core and the cladding have a different refractive index n : specifically, the cladding has a smaller refractive index. The total internal reflection that follows is generated by a wider incident angle than the critical angle θ_c .

The acceptance angle θ_a , defined as the maximum angle of entering light, lets us define the **numerical aperture (NA)**. It is defined as the sine of the largest angle an incident beam can have for total internal reflectance in the core and it is considered as the capacity of the fibre.

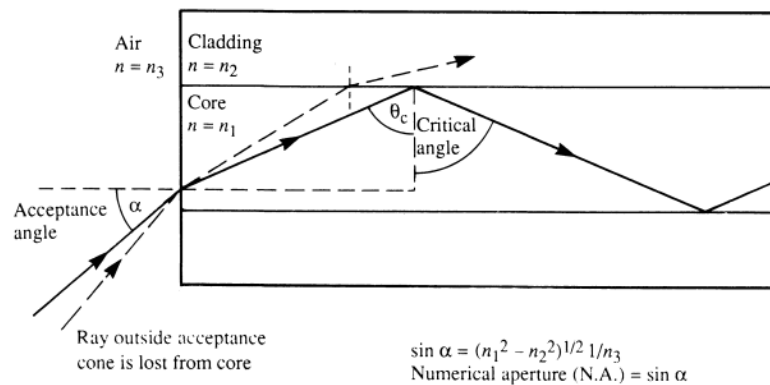


Figure 3.3: Propagation of light between the complex core-cladding thanks to the different refractive index. [ref_index]

Light is attenuated by different phenomena: *absorption* and *scattering*. The

medium itself, the silica, has impurities that causes attenuation. Scattering, instead, consists of the interaction between photons and the matter (in our case biological tissue will be taken in analysis): due to the interaction, the light is deflected. Moreover, the collision ionize the atoms that the target is made of and when they return to the ground state emit a photon.

We can distinguish three kind of optical fibre according to the **mode**: it describes the field of propagation of electromagnetic waves.

- **Single-Mode Optical Fibre**: this fibre is also called mono-modal because it supports only one mode. A typical configuration is with a core diameter between 8 - 10 μm , and the cladding 125 μm : the small diameter of the core ensure less attenuation plus a larger bandwidth. Single mode fibres are usually used to transmit signals on long distances.
- **Multi-Mode Optical Fibre**: core diameter is larger, greater then 10 μm . This feature lets more modes to propagates at the same time because of *modal dispersion*. Due to dispersion, the multi-mode fibre bandwidth–distance product limit is lower and the application is limited for distance shorter then kilometer.

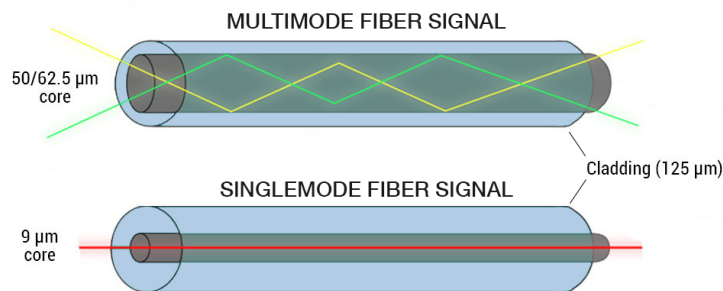


Figure 3.4: Different signals propagation between single-mode and multi-mode fibre. [17]

On the market can also be found **special-purpose fibre** that are designed with a non-cylindrical core or cladding layer. They are usually assembled to obtain certain features that cannot be granted by other types.

3.4 Optical Parameters

In order to understand better how laser interacts with matter, here a brief explanation of scattering and absorption phenomena is given. Both phenomena contributes to attenuation.

Absorption occurs when particles convert part of the energy of the incident ray in other forms of energy; instead, if part of the energy is diffused in all the directions we talk about *scattering*.

In absorption the energy of the wave is converted usually in vibrations that generate thermal energy; the effect depends on the medium and the absorption coefficient lets define how much a tissue will absorb. It is defined as:

$$\mu_a = N_a \sigma_a (m^{-1}) \quad (3.1)$$

where N_a is the density of particles that absorbs per volume unit (cm^{-3}) and σ_a is the cross-section (m^2), a measurement of the probability that the phenomenon will occur. Replacing μ with μ_a in the equation 2.3 the behaviour of tissue characterized by absorption only is described.

Scattering instead induces the deflection of the direction of propagation of the beam: it depends on the morphology of the tissue. Two kinds of scattering can occur: *elastic scattering* and *inelastic scattering*. In the first case the total kinetic energy of the system is conserved so the wavelength of the emitted beam is the same as the incident; in the second, the energy loss results in a change after the collision of the wavelength of the emitted radiation.

There are two types of elastic scattering:

- **Rayleigh scattering:** when the particles diameter is less than one-tenth the wavelength of incident light. Lights diffuse in every direction (*isotropic dispersion*);
- **Mie scattering:** when the particles have a dimension of the same order of magnitude or bigger then the wavelength of incident wave. In this case the diffusion is *anisotropic*.

The discerning parameter is $\alpha = \frac{2\pi R_p}{\lambda}$, where R_p is the particle radius, λ is the beam wavelength: if $\alpha \ll 1$ the former will occur; otherwise ($\alpha \simeq 1$) the latter.

When scattering takes place, a small percentage of light performs the **Raman Scattering**. It is an inelastic type of scattering where lights is diffused either with less energy, and this is called *Stokes Raman diffusion* or with more energy and is defined *anti-Stokes Raman diffusion*. Raman scattering is linked to the degree of polirization of molecules.

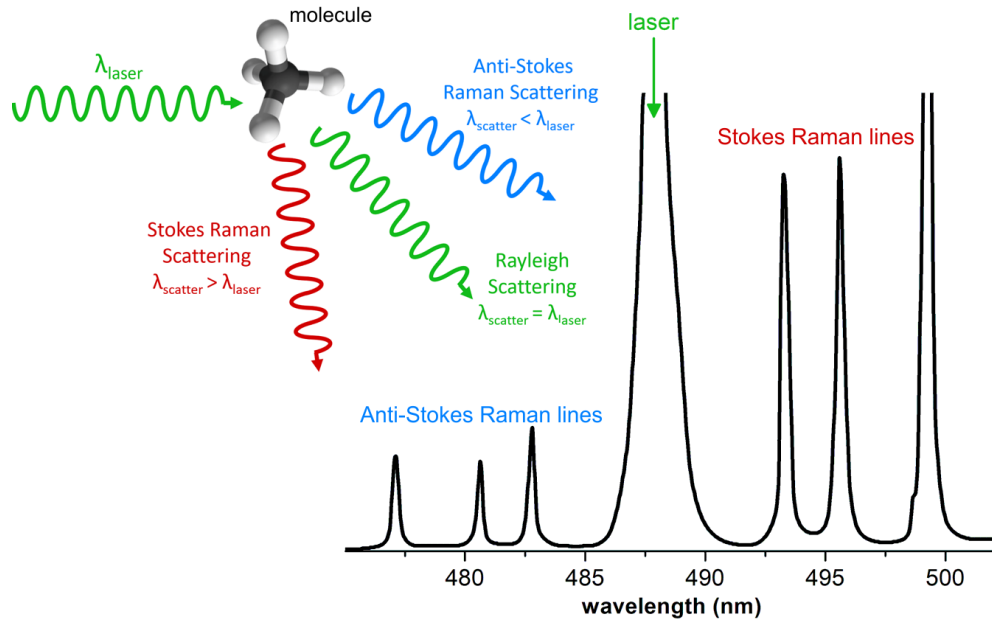


Figure 3.5: Scheme of Raman Scattering [18]

3.5 Interaction between laser and biological tissue

The property of absorption of tissues is defined by the bio-molecules that they are made of. As we said in (2.4), *chromophores* help to quantify the optical absorption of a tissue.

The most visible molecules are DNA, proteins, melanin, hemoglobin and water, whose characteristics change with the wavelength of the incident beam.

In spectrum of UV (180 to 400 nm) the predominant chromophores are protein, DNA and melanin.

In the spectrum of visible light (400 - 780 nm) the main contribution is given by melanin and hemoglobin.

Infrared spectrum goes from 0.78 μm to 1000 μm and has 5 sub-spectra: near infrared, short-wavelength , mid-wavelength, long-wavelength infrared (in the same order: IR, SWIR, MWIR), far-infrared (FIR). Here hemoglobin, water and proteins give the biggest contribution to absorption. The laser we have used for *ex-vivo* liver ablations works at 914 nm, so in the bandwidth of IR light.

Absorption increases with the wavelength. [20]

To understand better the effect of laser on the target is fundamental to know the type of interaction induced and where the process happens. In Fig. 3.7 one

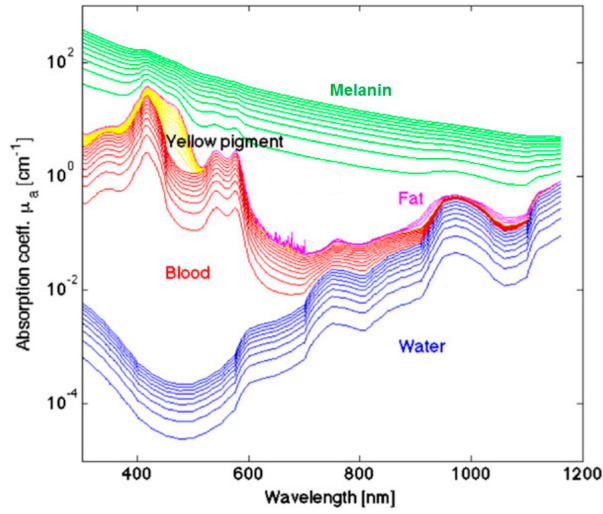


Figure 3.6: Absorbance of tissues at different wavelength.[19]

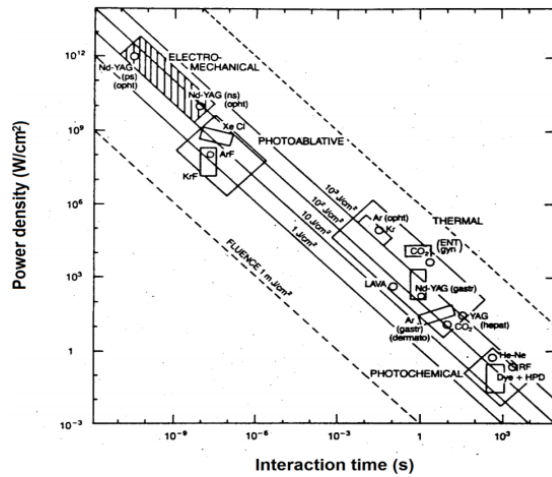


Figure 3.7: "Medical laser interaction map." [21]

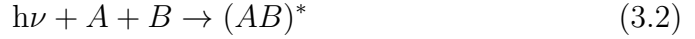
possible way to classify interactions is shown, considering the relationship between the power density (W/cm^2) and the time of exposure: it is called "*medical laser interaction map*" [21].

The map describes how target absorb selectively the energy without damaging the surrounding tissues. As a first approximation biological tissue can be considered isotropic and homogeneous - we used this approximation also to study a computational model. What is taken in account is reflection, absorption, scattering.

The irradiation is described by the diagonal lines, which are associated to a

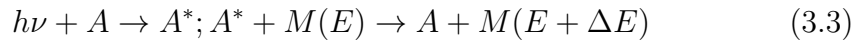
constant fluence (J/cm^2). Changing wavelength and time of exposure there will be four types of different nature interactions:

- **Photochemical interaction:** when the energy of the beam is greater than the chemical energy bond. It usually happens when the time of interaction is long (more than a second) and the intensity is lower (around $1 W/cm^2$). The energy induces a change in the structure of the molecules according to the reaction



where AB^* is an excited complex of A and B. This kind of emission, is used to achieve diagnosis with a very low probability of thermal damage or perforation of healthy tissue. UV radiation is used. On the other hand data must be collected real-time, so there is no way to make any evaluation of the area of extension of the disease.

- **Photothermal interaction:** when the energy of the beam is lower than the binding energy. IR lasers are used to achieve power densities around $100 W/cm^2$ both in continuous wave (CW) or pulsed wave (PW). The reaction takes place in two stages:



where A is the chromophore that is carried into an excited rotovibrational state by an IR photon. It is then de-excited by the surrounding molecules that increase their kinetic or thermal energy absorbing chromophore's energy. The effect of heating is related to the temperature, as we said in (tabella). Scar tissue replaces denatured cellular material. This kind of treatment is used for eye surgery or dermatology treatments. Above $100^\circ C$ water starts to evaporate and the dehydration of tissue causes a fast increase in the temperature up to $300^\circ C$ and the consequence is carbonization. It is important to control the fast rising to limit the damage of adjacent tissue. [22]

- **Photoablative interaction:** when the power density is very high ($10^7 - 10^{10} W/cm^2$) with a pulse duration from 10 to 100 ns the effect of the laser is a dissociation of molecules that can either have thermal effect or not. Since many biomolecules strongly absorb in the bandwidth of the visible light and UV the radiation leads to ionization, formation of plasma and removal of compounds of the target.



the removal of clusters of tissue is caused by the final expulsion of photoproduct at supersonic speed. The curve of ablation rate describes the effect of photoablation: ablation threshold is the limit above which the effect is of tissue removal and below heating.

- **Electromechanical interaction:** when a pulsed laser hit molecules with a power density greater than $10^{10}\text{W}/\text{cm}^2$. Immediately ionization is induced and the molecules generate plasma which itself causes cavitation: this phenomenon generates the formation of vapor bubbles that implode causing a pressure wave that follows the equation:

$$P_M = 12.3 \left(\frac{I_L}{10^{14}} \right)^{\frac{2}{3}} \lambda^{-\frac{2}{3}} \left(\frac{A}{2Z} \right)^{\frac{1}{3}} \quad (3.5)$$

where I_L is the intensity of the laser, λ the wavelength, A and Z are respectively the atomic mass and the atomic number of the target.

There is not a propagation of heating since the diffusion effect is limited: the treatment is limited to the spot. This treatment is typical for lithotripsy.

In 3.1 the effect of temperature on tissue is presented:

Temperature (°C)	Effect on tissue
$T < 45$	Change in cellular conformation (reversible)
$45 \leq T < 50$	Reduction of enzyme activity
$50 \leq T < 60$	Coagulation & proteins denaturation
$60 \leq T < 80$	Collagen destruction
$80 \leq T < 100$	Extracellular vacuoles formation
$T > 100$	Vaporization of water & destruction of extracellular vacuoles
$T > 300$	Carbonization

Table 3.1: Effects of temperature on biological tissues. [23]

Above 50 °C all the effects are irreversible since denaturation of proteins occur.

Chapter 4

Fibre Bragg Gratings (FBGs)

In-fibre Bragg Gratings (FBGs) belong to the class of optical fibre sensors (OFS) which are integrated in the fibre itself and let to measure and monitor many physical quantities. These sensors offer a wide range of advantages considering they don't need electric energy to work.

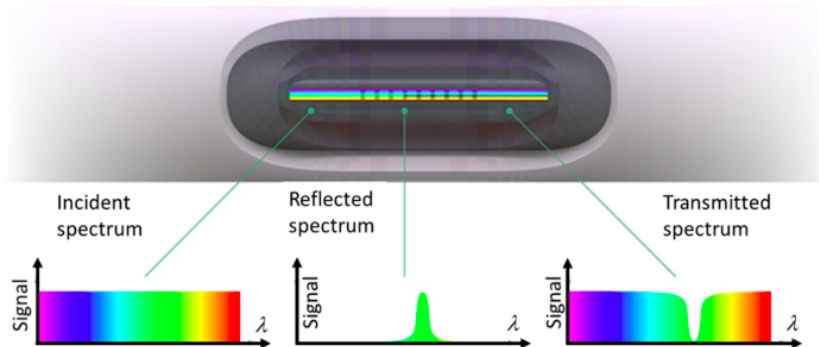


Figure 4.1: Operating Principle of Fibre Bragg Gratings [24]

In this thesis FBG have been used to measure temperatures, therefore here a focus on this sensor is given. They are made by periodically modulating the refractive index of the fibre core; the principle of functioning is based on the Bragg law that analyze the condition of constructive interference for crystals:

$$2d \sin \theta = n\lambda \quad (4.1)$$

d is the distance between two adjacent planes, θ the incident angle, n an integer

and λ the wavelength.

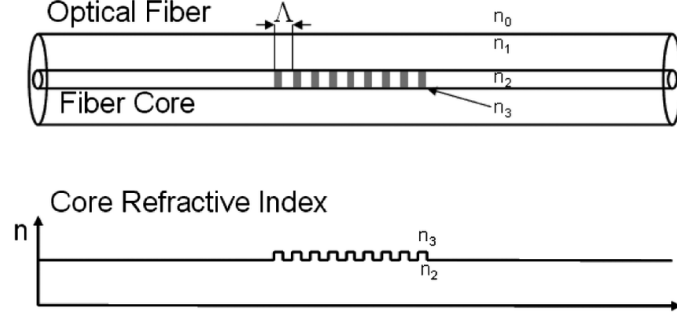


Figure 4.2: FBG structure Inside the Optical fibre

While the light passes through the fibre it is weakly reflected by each grating plane: the different reflections sum up in a constructive or destructive interference depending on whether the wavelengths satisfy or not the equation 4.1. Adapting the abovementioned equation for silica: this develop let to define the parameter that characterize an FBG: the **Bragg wavelength**:

$$\lambda_B = 2n_{\text{eff}}\Lambda \quad (4.2)$$

where n_{eff} is the refractive index of the core and Λ the periodicity of the grating: any changing of this factor will shift the reflected spectrum. Temperature and strain variations affect this parameter.

Starting from the infinitesimal variation of Bragg wavelength:

$$\begin{aligned} d\lambda_B &= \left[\frac{\delta}{\delta\varepsilon} 2n_{\text{eff}}\Lambda \right] d\varepsilon + \left[\frac{\delta}{\delta T} 2n_{\text{eff}}\Lambda \right] dT \\ &= \left[2n_{\text{eff}} \frac{\delta\Lambda}{\delta\varepsilon} + 2\Lambda \frac{\delta n_{\text{eff}}}{\delta\varepsilon} \right] d\varepsilon + \left[2n_{\text{eff}} \frac{\delta\Lambda}{\delta T} + 2\Lambda \frac{\delta n_{\text{eff}}}{\delta T} \right] dT \end{aligned} \quad (4.3)$$

Since the interest is focused on the relative phase difference 4.3 has to be divided by λ_B as defined in 4.2:

$$\frac{d\lambda_B}{\lambda_B} = \left[\frac{1}{\Lambda} \frac{\delta\Lambda}{\delta\varepsilon} + \frac{1}{n_{\text{eff}}} \frac{\delta n_{\text{eff}}}{\delta\varepsilon} \right] d\varepsilon + \left[\frac{1}{\Lambda} \frac{\delta\Lambda}{\delta T} + \frac{1}{n_{\text{eff}}} \frac{\delta n_{\text{eff}}}{\delta T} \right] dT \quad (4.4)$$

This equation 4.4 shows that the Bragg wavelength relative shift is both influenced by strain (first part of the equation) and by the temperature variation. The integration of 4.4 allows to expand the solution to the *finite* case:

$$\Delta\lambda_B = K_\varepsilon \cdot \varepsilon + K_T \cdot T \quad (4.5)$$

where:

$K_\epsilon = 1\text{pm}/\mu\epsilon$ is strain sensitivity;

$K_T = 10\text{ pm}/^\circ\text{C}$ is the temperature sensitivity. [25]

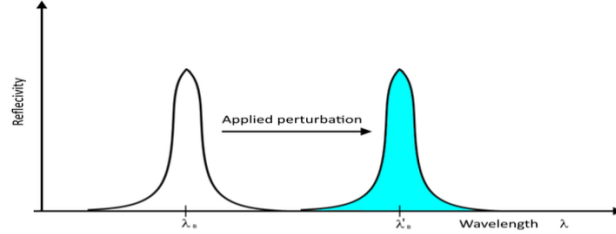


Figure 4.3: Spectrum Shift After an External Perturbation.

4.1 Manufacture

To fabricate Fibre Bragg Gratings usually the fibre is exposed to UV laser light. Some methods used to write the FBGs are called off-line methods since they are used after the fabrication of the optical fibre. To achieve the submicron periodic pattern three main techniques are used:

- **Interferometric Technique:** the refractive index modulation is achieved using an interferometer "which splits the incoming laser beam into two beams and then recombines them to form an interference pattern". [26] The equation below gives the spatial period

$$\Lambda = \frac{\lambda_{UV}}{2\sin(\theta/2)}$$

where Λ_{UV} is the wavelength of the two writing beams and θ is the angle between them which allow to have a good range of wavelength for the FBGs inscribed.

- **Point by Point Technique:** each grating plane is made by an excimer laser with a single focused pulse. As well as for the interferometric technique an UV light is used: a focusing lens impress the slit on the core and with the irradiation the refractive index is locally increased. Then the fibre is moved parallel to its axis of a quantity Λ equal to the grating pitch.
- **Phase Mask Technique:** this method is widely used since it let to obtain many different patterns. "The phase-mask is a diffractive optical element that spatially modulates the UV laser writing beam" [26] and can be performed

holographically or by electron-beam lithography. The mask is made in fused silica, which is transparent to UV; the pattern on the mask defines grating pitch. The FBGs used in this master thesis have been written with this technique but using femtosecond pulsed laser. It emits optical pulses with a duration below 1 ps.

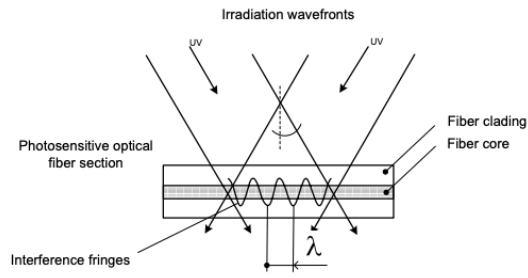


Figure 4.4: Simplified Scheme of the Interferometric Method [26]

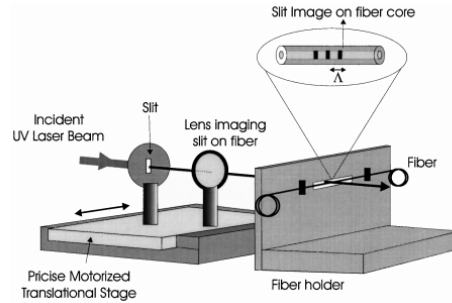


Figure 4.5: Set Up for point-by-point technique. [26]

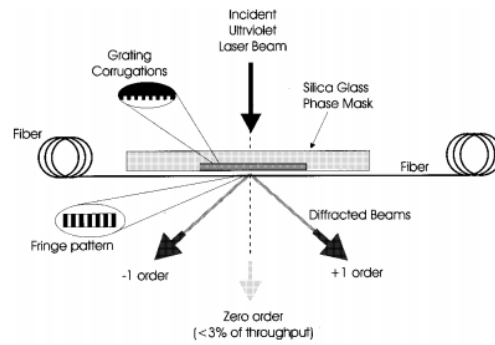


Figure 4.6: Scheme of the Phase Mask Method to imprint gratings in a photosensitive optical fibre. The diffracted plus and minus first orders are maximized. [26]

4.2 Classification

Fibre Bragg Gratings can be classified according to the the grating period or the refractive index.

Considering the grating period there are four types of FBG:

- **Uniform:** this is the simplest form: the index modulation is constant in amplitude and period therefor the Bragg wavelength is constant;

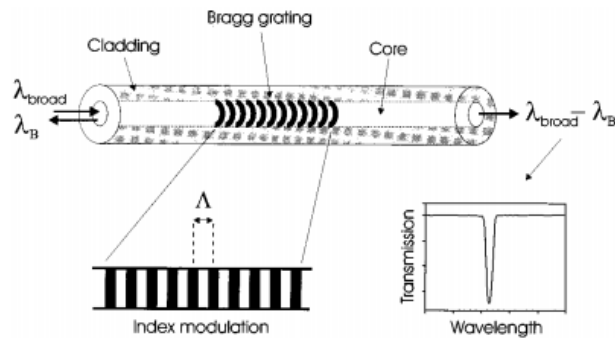


Figure 4.7: Uniform Bragg Grating Illustration.

- **Chirped:** the grating changes monotonically. It can be obtained modifying the grating period Λ , the refractive index of the core or both;

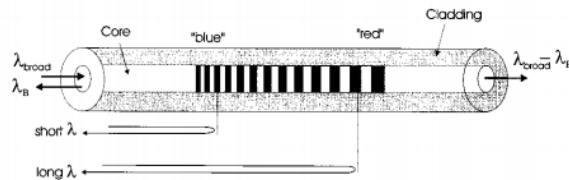


Figure 4.8: Chirped Bragg Grating Illustration.

- **Tilted:** or *blazed*. The refractive index modulation is not perpendicular to the fibre axis, but angled; the result is a multiple direction patten for the guided light;
- **Superstructure:** the grating is obtained with a modulated exposure.

For what concerns the refractive index it has two main parameters: the profile and the offset. The first can be *uniform* or *apodized*, that means that the gratings

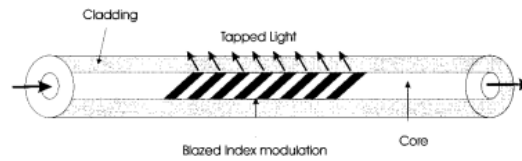


Figure 4.9: Tilted Bragg Grating Illustration

have significant amelioration in the suppression of side lobes. FBGs can be classified according to this parameter in:

- **Uniform:** each line of the grating has the same refractive index;
- **Gaussian-Apozided:** each refractive indices has a gaussian-shaped profile;
- **Raised Cosine-Apozided:** the profiles of the refractive index is both higher and lower than the core refractive index;
- **Discrete phase shift:** the phase of the profile of the refractive index changes along the core. For this reason the shape of reflection is specular in relation to the Bragg Wavelength.

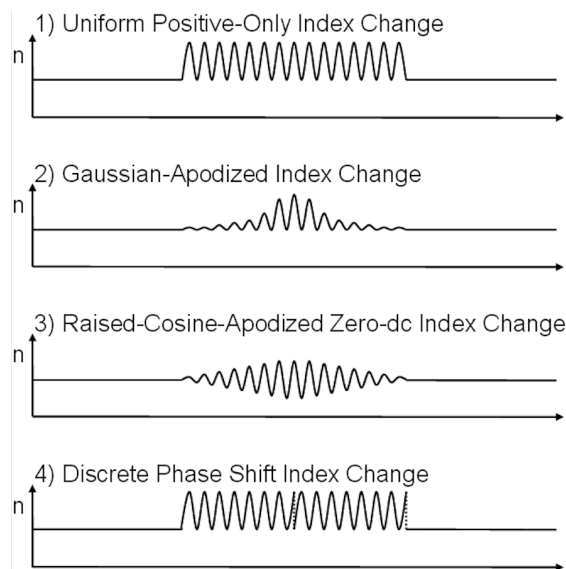


Figure 4.10: "Refractive index profile in the core of, 1) a uniform positive-only FBG, 2) a Gaussian-apodized FBG, 3) a raised-cosine-apodized FBG with zero-dc change, and 4) a discrete phase shift FBG." [27]

4.3 Optical Interrogator: MicronOptics

In general, all the interrogators used to acquire the signals from FBGs are made of two principal parts: the light source and an optical detector to analyze the reflected spectrum. The technique used for reading the spectra is called *wavelength division multiplexing* since the instrument measures the wavelength of each FBG and not the frequency. Furthermore, on the same optical fibre an entire array of FBGs can be interrogated at the same time since FBG grating has a different Bragg wavelength. There are two kinds of interrogators: the main difference is the source of light.

In the first case (Fig. 4.11) the source is usually a LED since its bandwidth can

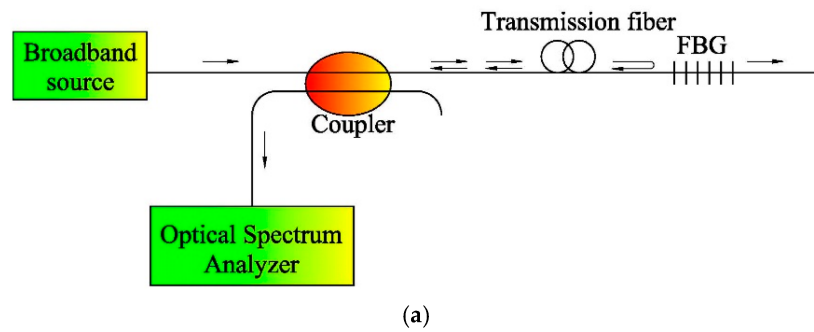


Figure 4.11: Broadband source Interrogator. [28]

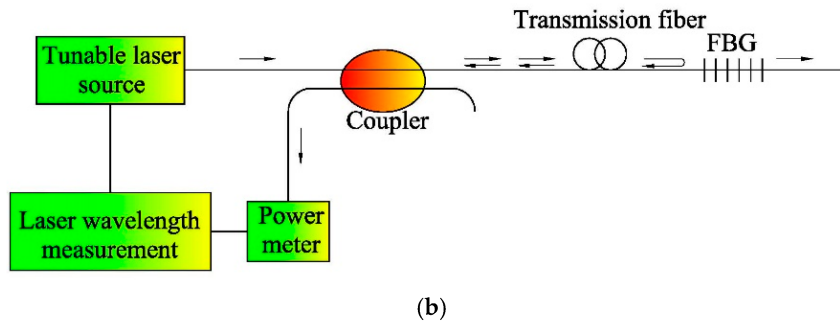


Figure 4.12: Tunable Laser. [28]

be modulated easily. The light passes through an *optical circulator* and reaches the FBGs; then the optical circulator as well guides the reflected light to a *tunable filter*. The band-pass filtered signal goes in input to an optical detector, then to a trans-impedance amplifier to convert the optical power into an analogic voltage. The second one (Fig. 4.12) is the principle of working of Micron Optics. In this case the source of light has a narrow band, therefore there is no implication of the

band-pass filter. The optical interrogator directly "send" the reflected signal to the photodiode that converts the light into an analog voltage.

During our experiments the Micron Optics HYPERION si155 (Fig. 4.13) by Luna Technologies has been used.



Figure 4.13: Micron Optics HYPERION.

The technical specifications are:

- **Wavelength Range:** 1500-1600 nm;
- **Wavelength Resolution:** 10pm;
- **Maximum Acquisition Rate:** 10 Hz for spectrum detection, 1kHz for peak detection;
- **Four Parallel Channels.**

In order to work properly, the instrument must be connected to the same Ethernet line of the device used for user interface. The software is called *ENLIGHT Sensing Analysing Software*.

The signal of each optical fibre connected to one of the four channel can be visualized with the software: they can be visualized all together or one per time. The interface also shows the number of FBGs detected on each channel.

The Bragg peak wavelength detection is automatic: the instrument has an algorithm based on the *zero crossing* method.

The signal is first filtered with a *derivative filter*. The output has more zeros than the original real signal therefor in necessary to set a threshold value: the wavelength range corresponding to the signal that exceed the threshold is now the space where the zero crossing method is applied.

Part II

Experimental Trials

Chapter 5

Characterization of FBG array Sensors

In this master thesis the use of FBGs was fundamental to determinate the temperature distribution during *ex-vivo* liver ablation.

Characterize the fibre Bragg gratings means to find the relationship that links the acquired data the physical quantity of interest; in this specific test data acquired are the wavelengths using Micron Optics HYPERION and the temperature sensed by the termocouple during the entire test; the physical quantities are the two parameters in the Bragg equation. The equation that relates these two parameters is:

$$\lambda_B = \lambda_0 + kT \quad (5.1)$$

where λ_B is the Bragg Wavelength -measured-, λ_0 is the reflected peak positioning at 0 °C and k is the temperature sensitivity in pm/°C. A greater sensitivity means a wider λ_B for a given temperature variation.

Two factors distinguish the array of FBGs used for the thesis:

- the distance between the centers of the gratings;
- the positioning respect to the core.

The first array is straight: all the gratings are equally spaced on the core axis, therefor they are distributed on a larger length Fig. 5.1 ; FBGs of the second array are instead staggered in respect to the axis and the centers are closer Fig. 5.2

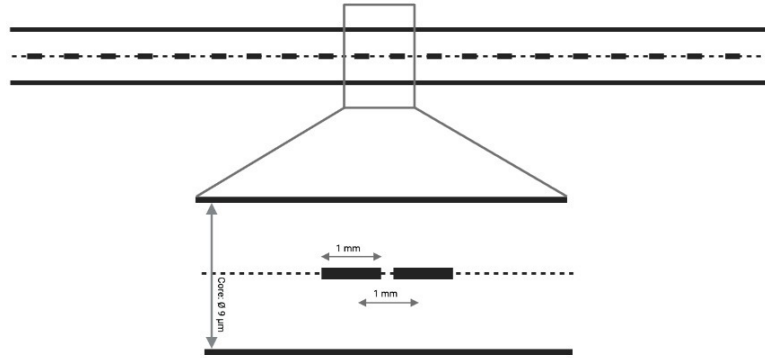


Figure 5.1: Scheme of the straight array and a zoom

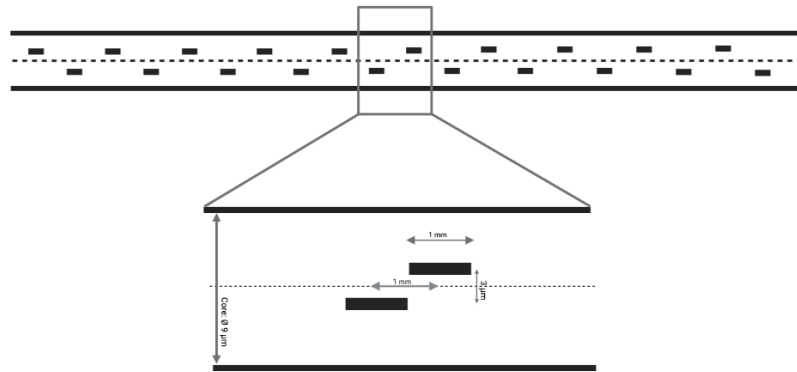


Figure 5.2: Scheme of the ultra dense array and a zoom

5.1 Set up and Measurements

To achieve the FBGs characterization the instruments needed are:

- **Optical Interrogator MicronOptics HYPERION si155:** specifics described in (). Sampling rate 1 Hz, data saved in a txt file;
- **J-type Thermocouple:** National Instrument (NI) thermocouple used with the USB-TC01 that has an instantDAQ technology. The instantDAQ has an integrated software that allows to show data acquired from the thermocouple device in real-time and save them in txt file. It can be connected through an USB port to any computer. The features of a generic J-type thermocouple are:
 - Resolution: 0.0625 °C;

- Temperature error: less than 1.5 °C;
- Maximum sample rate: 4S/s;
- ADC resolution: 20bits.

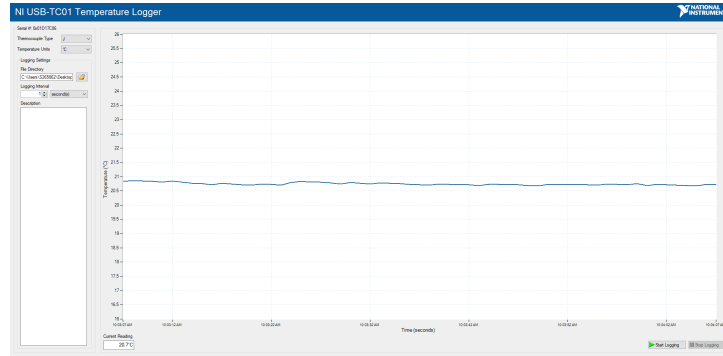


Figure 5.3: Software interface of thermocouple launcher.

- **Heating plate;**
- **Metallic block:** it has a high thermal inertia. This help having FBGs sensing the temperature of the metallic bloc and reduce oscillations;
- **Insulating block:** the metallic block is covered with a block of insulating material. Before in has been properly grooved to cover capillaries and thermocouple;
- **two FBGs arrays:**
 - Straight array, written on a single mode fiber
 - * Core diameter 9 μm ;
 - * Cladding diameter 125 μm ;
 - * 1 mm between FBGs centres;
 - * 1 mm extension for each FBG;
 - * FBGs on the same axis in the core;
 - High-density array, written on a single mode fiber
 - * Core diameter 9 μm ;
 - * Cladding diameter 125 μm ;
 - * 1 mm between FBGs centres;
 - * 1 mm extension for each FBG;
 - * FBGs alternated on 2 parallel axes in the core;

- **Glass capillary:** type Q051:
 - Material: quartz;
 - Outside diameter: 0.5 mm ;
 - Inside diameter: 0.126 mm;

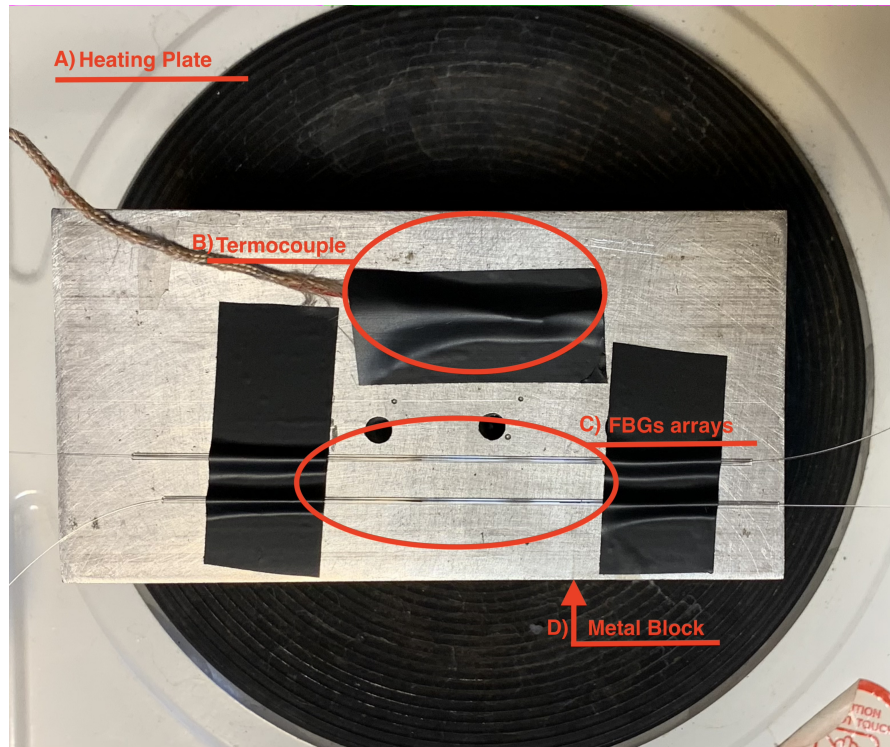


Figure 5.4: Set up for the FBGs characterization. A) is the plate used in the heating process of the D) metal block. B) Termocouple and C) FBGs array stick to the block with insulating plate. C) is covered in glass capillaries.

First of all, MicronOptics is turned on to ensure the stabilization of the instrument before the tests get started and the thermocouple is connected to the USB of the pc. Each optical fibre is connected respectively to channel 1 and channel 2 of the MicronOptics. Both FBGs, the "straight" and the ultradense, are placed in the capillaries to prevent any effect of strain on the measurements. Thermocouple and the capillaries are fixed to the thermocouple with insulating tape: the sensing tip of the thermocouple is completely cover to guarantee the contact with the metallic block for the whole experiment. (Fig. 5.4).

After the positioning, the whole set up is covered with the insulating block to ensure that any variation of temperature in the room, or the air moving could change the temperature sensed by the FBGs. The sampling rate of both ENLIGHT and TC01 software are set at 1Hz: since the experiment takes very long time this sampling rate suites correctly the purpose.

The heating plate is now turned on until the temperature registered by the thermocouple is around 40-50 °C: in this way the system will reach a temperature around 100°C and starts cooling. For the characterization the cooling process is more relevant for its slowness, therefor the results are more reliable.

The recordings are stopped when the system is at room temperature.

5.2 Results and Conclusions

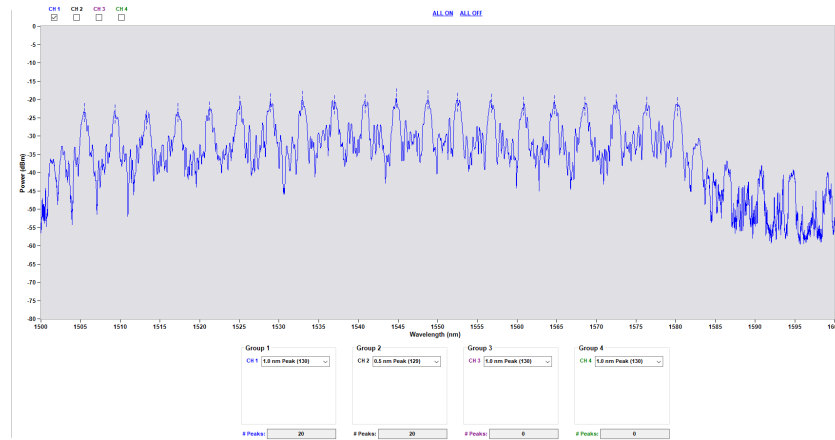


Figure 5.5: Interface of the software ENLIGHT while the straight array was connected.

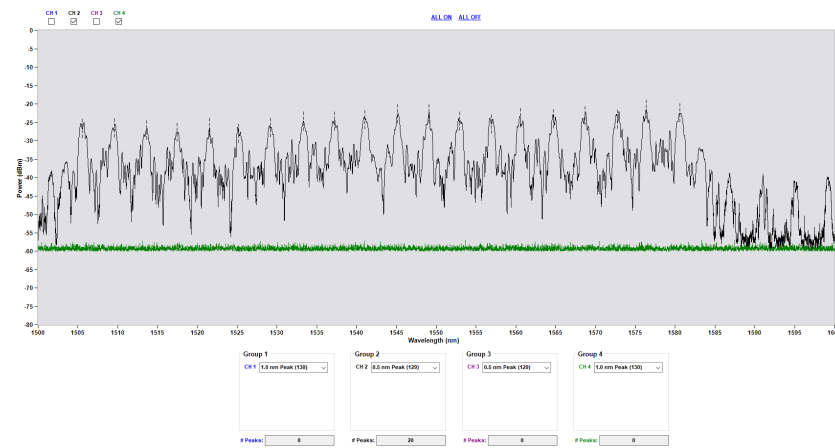


Figure 5.6: Interface of the software ENLIGHT while the ultradense array was connected.

The data acquired are then processed in MATLAB[®](A.1). To reduce the noise, signals are filtered with a FIR filter that average a number of samples acceptable for the thermocouple and MicronOptics recording. The function used for filtering is `filtfilt` to avoid a phase distortion. Time axes are then aligned to relate the temperatures recorded and the corresponding Bragg wavelengths: at this point the data are cut considering only the slope.

The function `polyfit` extracts the parameters into a matrix.

In the following tables (5.1) (5.2) results are presented:

	FBG1	FBG2	FBG3	FBG4	FBG5	FBG6	FBG7
λ_0 (nm)	1505.1	1509.1	1512.9	1516.9	1520.9	1524.6	1528.6
k_T (nm/°C)	0.0122	0.0123	0.0123	0.0123	0.0123	0.0123	0.0123

	FBG8	FBG9	FBG10	FBG11	FBG12	FBG13	FBG14
λ_0 (nm)	1532.6	1536.6	1540.5	1544.4	1548.4	1552.2	1556.4
k_T (nm/°C)	0.0124	0.0125	0.0125	0.0125	0.0126	0.0126	0.0126

	FBG15	FBG16	FBG17	FBG18	FBG19	FBG20
λ_0 (nm)	1560.4	1564.3	1568.2	1572.1	1575.9	1579.8
k_T (nm/°C)	0.0126	0.0127	0.0127	0.0128	0.0128	0.0128

Table 5.1: λ_0 and k_T values for each FBG. Straight.

	FBG1	FBG2	FBG3	FBG4	FBG5	FBG6	FBG7
λ_0 (nm)	1505.3	1509.3	1513.3	1517.2	1521.2	1524.9	1528.9
k_T (nm/°C)	0.0108	0.0108	0.0108	0.0109	0.0109	0.0109	0.0110

	FBG8	FBG9	FBG10	FBG11	FBG12	FBG13	FBG14
λ_0 (nm)	1533.1	1536.9	1540.8	1544.9	1548.8	1552.7	1556.7
k_T (nm/°C)	0.0110	0.0111	0.0111	0.0111	0.0111	0.0112	0.0112

	FBG15	FBG16	FBG17	FBG18	FBG19	FBG20
λ_0 (nm)	1560.3	1564.5	1568.4	1572.4	1576.1	1580.3
k_T (nm/°C)	0.0112	0.0112	0.0113	0.0113	0.0113	0.0113

Table 5.2: λ_0 and k_T values for each FBG. HD

Since the sensitivity k only depends on the material, its value is between 10 and 20 pm/°C for both straight and ultra dense array. We can see that for the straight array sensitivities are a little bit greater respect to the ultradense array: this may depend on the conditions when they have been written. To determine the quality of the characterization, calibration lines that compare the interpolating lines and the real Bragg wavelengths acquired have been plotted.

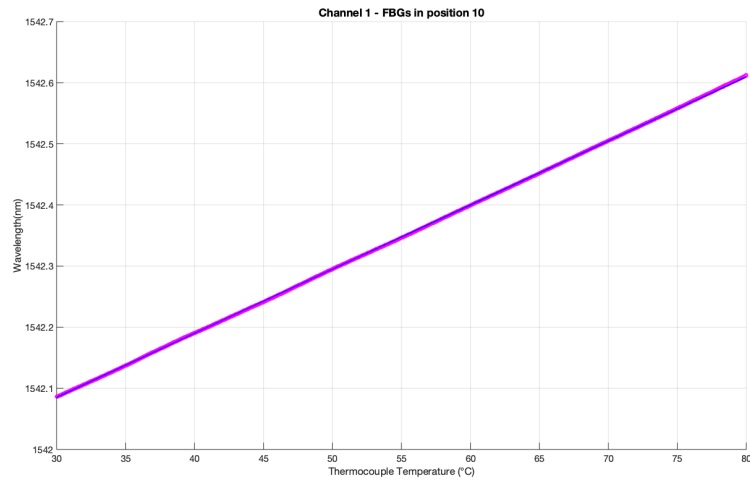


Figure 5.7: Calibration line: in blue the interpolating line is presented, in magenta the recorded data. Straight array.

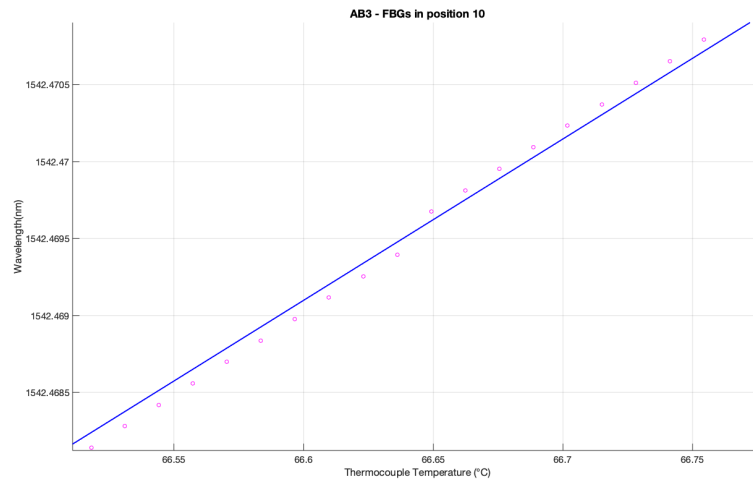


Figure 5.8: Zoom of the calibration line: the point recorded overpass the interpolating line. Straight array.

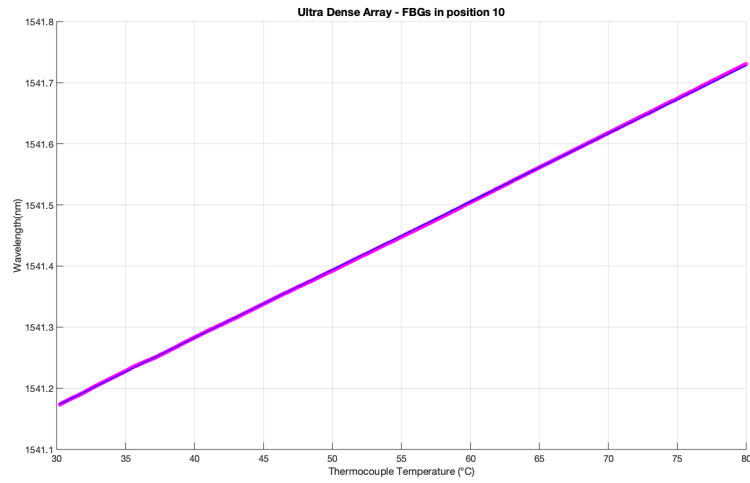


Figure 5.9: Calibration line: in blue the interpolating line is presented, in magenta the recorded data. Ultradense array.

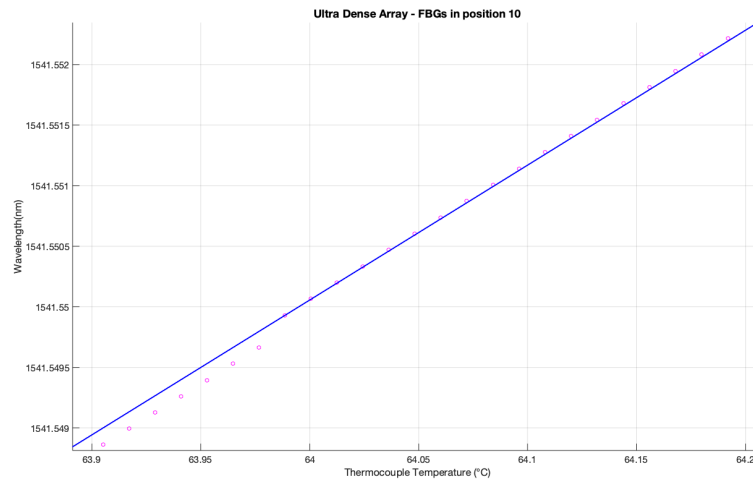


Figure 5.10: Zoom of the calibration line: the point recorded overpass the interpolating line. Ultradense array.

The interpolation line and the scatter-plot representing the acquired wavelengths doesn't show any particular difference, which is encouraging for the results obtained for the characteristic parameters.

Below tables reporting the maximum relative error for each FBG and the maxima deviations help to see the final results. The maximum deviation has been obtained dividing the difference between the measured and the calculated wavelengths for the sensitivity of the FBG, therefore the dimension is °C; the relative error has been evaluated dividing the difference between the measured and the calculated value for the measured value and the result is adimensional.

	FBG1	FBG2	FBG3	FBG4	FBG5	FBG6	FBG7
$\Delta T_{\max}(\text{°C})$	0.411	0.366	0.199	0.171	0.225	0.245	0.274
Error	0.0107	0.0057	0.0064	0.0042	0.0097	0.0063	0.0060

	FBG8	FBG9	FBG10	FBG11	FBG12	FBG13	FBG14
$\Delta T_{\max}(\text{°C})$	0.202	0.169	0.197	0.182	0.236	0.218	0.174
Error	0.0070	0.0063	0.0045	0.0039	0.0034	0.0044	0.0063

	FBG15	FBG16	FBG17	FBG18	FBG19	FBG20
$\Delta T_{\max}(\text{°C})$	0.207	0.157	0.175	0.142	0.134	0.149
Error	0.0035	0.0027	0.0031	0.0044	0.0053	0.0047

Table 5.3: Maximum temperature variation during the descending thermal gradient and maximum relative temperature error for each FBG. Straight

	FBG1	FBG2	FBG3	FBG4	FBG5	FBG6	FBG7
$\Delta T_{\max}(\text{°C})$	0.197	0.208	0.179	0.169	0.243	0.269	0.239
Error	0.0045	0.0052	0.0034	0.0052	0.0037	0.0061	0.0071

	FBG8	FBG9	FBG10	FBG11	FBG12	FBG13	FBG14
$\Delta T_{\max}(\text{°C})$	0.246	0.210	0.230	0.171	0.159	0.218	0.212
Error	0.0049	0.0063	0.0076	0.0047	0.0048	0.0047	0.0044

	FBG15	FBG16	FBG17	FBG18	FBG19	FBG20
$\Delta T_{\max}(\text{°C})$	0.164	0.217	0.188	0.229	0.175	0.157
Error	0.0047	0.0056	0.0057	0.0058	0.0048	0.0061

Table 5.4: Maximum temperature variation during the descending thermal gradient and maximum relative temperature error for each FBG. HD

For what concerns the straight array we can see that the maximum error in estimating the temperature is below half a degree centigrade: the maximum calculated shift is for the first FBG and is equal to 0.411 °C. Another great result is for the relative error, which is maximum 1.07%, always for the first FBG.

In the case of the ultradense array things are even better with a maximum temperature shift of 0.269 °C and a relative error of 0.61%.

These measures helped understand the preciseness of our esteem during liver ablation, even though in that case there are more factors to take in account. Since sensors are not covered by any capillary, there is the possibility to introduce strain: the error increases. For the FBGs used in this master thesis the error due to strain is 10pm/°C.

Although the procedure of characterization takes some time, the simplicity of the set up and measurement evaluation doesn't require long computational time and complexity. Furthermore, FBGs would not be available without obtaining the linear relationship between the wavelength and the corresponding temperature.

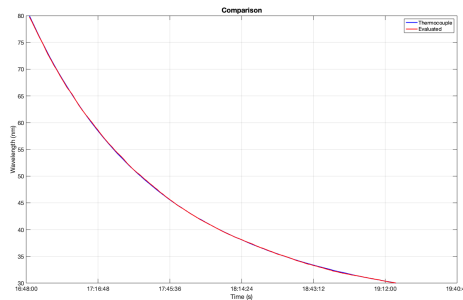


Figure 5.11: Comparison between the trends of the temperature measured by the thermocouple and evaluated by the straight array.

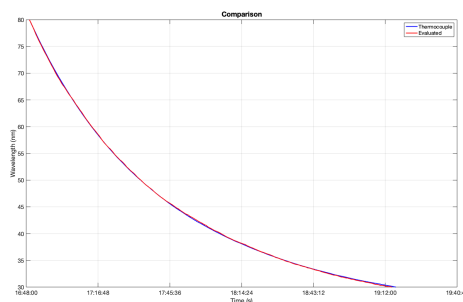


Figure 5.12: Comparison between the trends of the temperature measured by the thermocouple and evaluated by the ultradense array.

5.3 Evaluation of self-heating

After the characterization a self-heating evaluation has been done.

For every temperature sensor self-heating is an issue: the analysis was conducted to see the goodness of the future measurements on liver during ablation. Moreover, a stability test has been previously done to see the fluctuation of temperature values. Sensors have been tested both in air and water to see how the two different environments can affect the measure. Different level of power have been used.

5.3.1 Set Up and Measurement

In (5.5) the organization of the tests is presented.

Many values of power have been used for both environments to see if there is a relationship between temperature variations and the value of power supplied.

The instruments used are:

- **Two optical fibres with FBGs arrays;**
- **Thermocouple:** its use has been limited to see the room temperature;
- **MicronOptics HYPERION;**
- **LuOcean Mini 8 by Lumics:** laser with two high power diodes that can emit at two wavelength (915 nm and 1470 nm) both in the NIR bandwidth. The first value has been chosen. 5.13 Another diode is present that emits in the visible light spectrum used as a pointer. The laser was controlled with a LabView program ;
- **Delivery fibre:** NA 0.22;
- **Insulating structure:** to prevent laser diffusion all over the room.

TEST	POWER	ENVIRONMENT
1	Laser off	air
2	0.5 W	air
3	1 W	air
4	1.5 W	air
5	Laser off	water
6	0.5 W	water
7	1 W	water
8	1.5 W	water

Table 5.5: Organization of the tests performed to evaluate the self-heating effect.



Figure 5.13: Laser module used for evaluating the self-heating.

Now on I will refer to the tests with the numbers presented in 5.5. For the experiments from 1 to 4, a vice has been used to hold the optical fibre containing the FBGs to test: to reduce the effect of strain, the extremities of the section of fibre that contains the gratings are put in two capillaries (A), Fig. 5.14) used as a support. For the delivery probe was also used a support to guarantee safety and keep at a fixed distance the laser and the target for the whole experiment in air.

Before turning the laser on the set up was covered up with a protective shield that ensures no one was exposed to the laser light.

For the tests from 5 to 8 the set up was similar, except for the vice and the use of capillaries: the gratings of the fibre were totally immersed in the water therefore no support was necessary. The shield was used.

The tests with the laser off (1 and 5) lasted 180 seconds, with a sampling frequency for MicronOptics of 2 Hz: these tests helped us to set a minimum range of oscillations for the temperature sensed by the FBGs.

The tests with the laser turned on lasted 60 seconds, and the laser was turned on only for 10 seconds. It was not possible to set with LabView a timer, therefore a chronometer has been used to check that the laser was irradiating only for 10 seconds: as a consequence, each test may have at least 1 second error due to the instrument. The sampling frequency in this case was set at 5Hz.

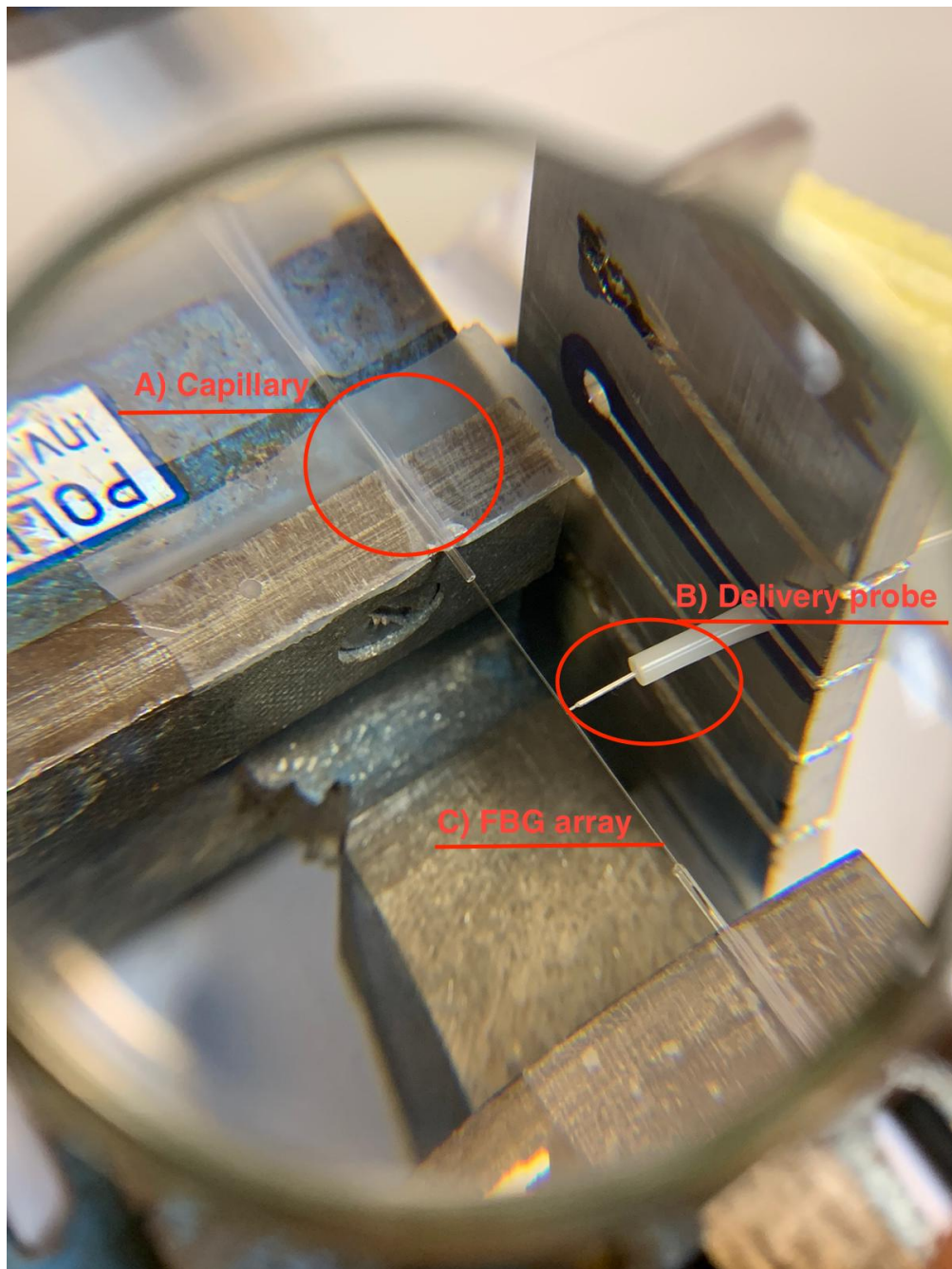


Figure 5.14: Self-heating evaluation in air. A) Glass capillary to reduce the effect of strain on the fibre containing the FBGs array. B) Delivery fibre for laser delivery. C) FBGs array

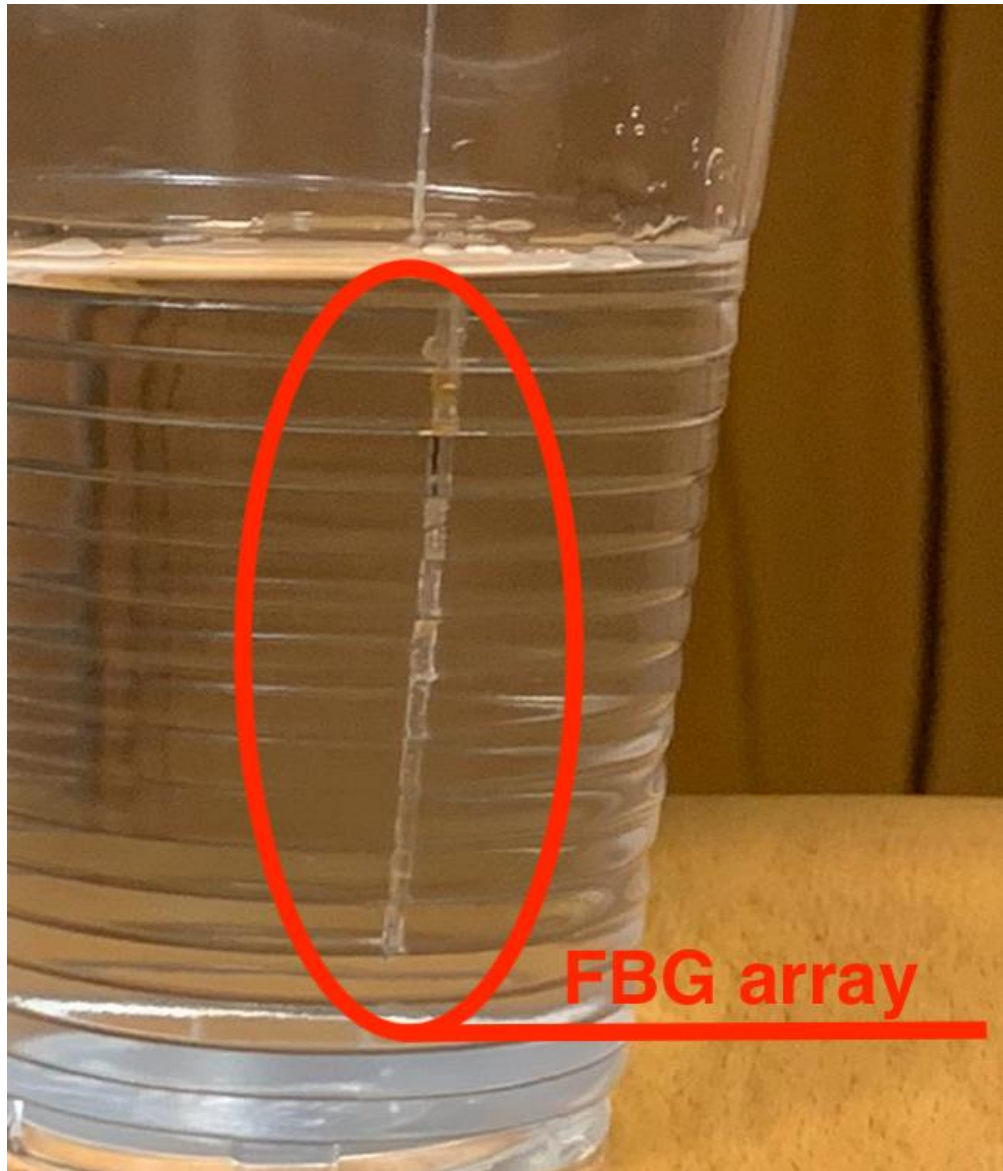


Figure 5.15: Self-heating evaluation in water: the array is completely immersed in water. The laser is applied from the outside.

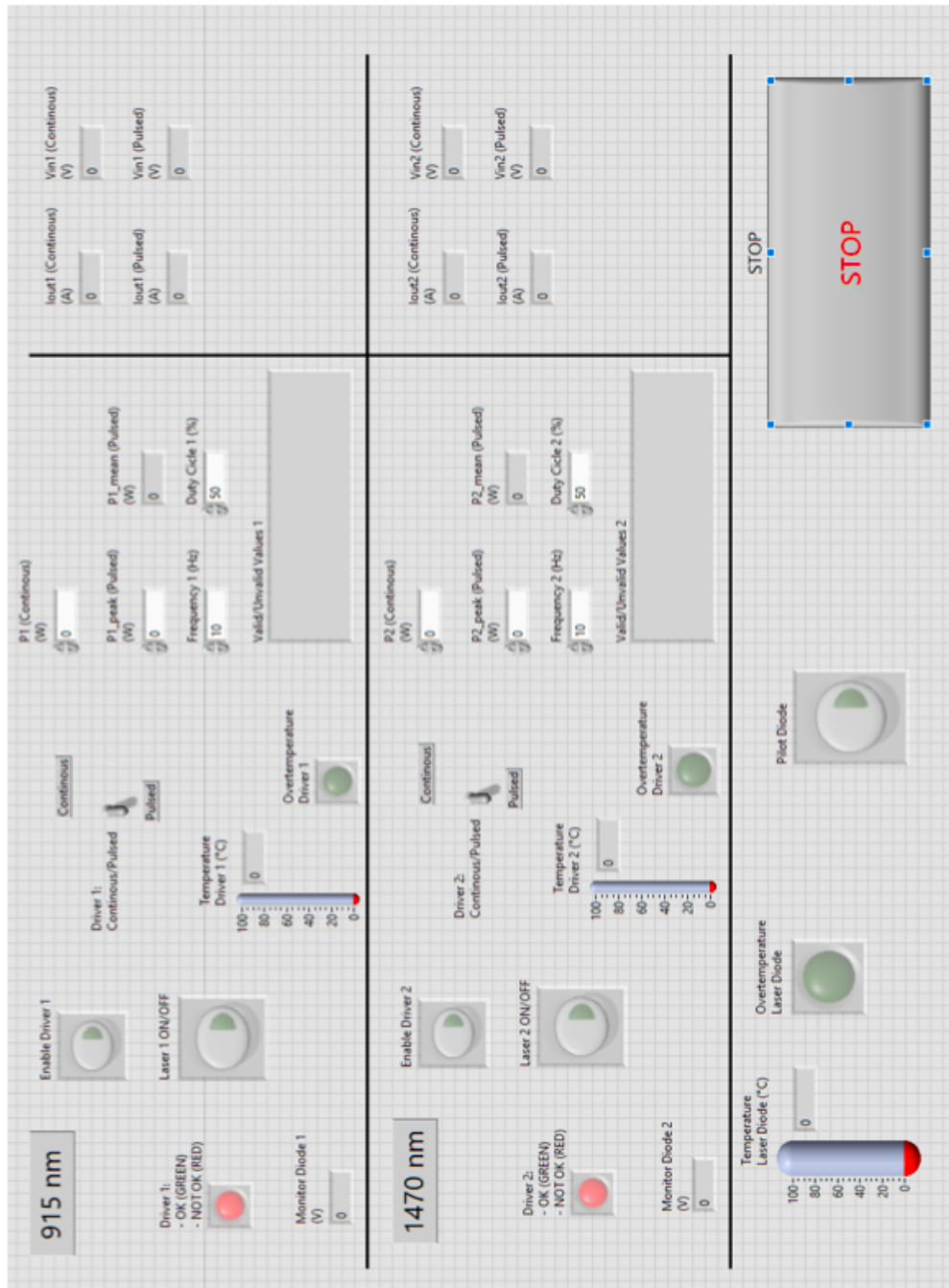


Figure 5.16: LabView interface to manage laser features. Two ways of emitting are possible: continuous and pulsed.

FBG	AIR			
	Laser off	0.5W	1W	1.5W
1	0.28 °C	0.23 °C	0.35 °C	0.47 °C
2	0.29 °C	0.30 °C	0.55 °C	0.87 °C
3	0.28 °C	0.53 °C	1.05 °C	1.47 °C
4	0.29 °C	1.11 °C	1.83 °C	2.57 °C
5	0.33 °C	1.29 °C	2.29 °C	3.01 °C
6	0.27 °C	0.62 °C	1.26 °C	1.60 °C
7	0.31 °C	0.39 °C	0.76 °C	1.06 °C
8	0.27 °C	0.18 °C	0.39 °C	0.56 °C
9	0.30 °C	0.20 °C	0.29 °C	0.29 °C
10	0.25 °C	0.21 °C	0.22 °C	0.30 °C
11	0.34 °C	0.21 °C	0.21 °C	0.25 °C
12	0.33 °C	0.19 °C	0.26 °C	0.36 °C
13	0.25 °C	0.21 °C	0.13 °C	0.25 °C
14	0.25 °C	0.19 °C	0.15 °C	0.19 °C
15	0.20 °C	0.20 °C	0.17 °C	0.17 °C
16	0.18 °C	0.12 °C	0.14 °C	0.17 °C
17	0.22 °C	0.16 °C	0.14 °C	0.16 °C
18	0.16 °C	0.12 °C	0.10 °C	0.12 °C
19	0.16 °C	0.15 °C	0.11 °C	0.16 °C
20	0.26 °C	0.11 °C	0.20 °C	0.15 °C

Table 5.6: Maximum temperature deviation for the FBGs in air during self-heating evaluation.

FBG	WATER			
	Laser off	0.5W	1W	1.5W
1	1.24 °C	1.19 °C	1.82 °C	2.50 °C
2	1.69 °C	1.42 °C	2.14 °C	2.94 °C
3	1.79 °C	1.30 °C	1.84 °C	2.46 °C
4	1.50 °C	1.27 °C	1.84 °C	2.59 °C
5	1.17 °C	1.10 °C	1.73 °C	2.51 °C
6	0.99 °C	0.96 °C	1.56 °C	2.04 °C
7	0.76 °C	0.92 °C	1.27 °C	1.95 °C
8	0.70 °C	0.78 °C	1.13 °C	1.73 °C
9	0.53 °C	0.67 °C	1.08 °C	1.54 °C
10	0.44 °C	0.66 °C	1.04 °C	1.54 °C
11	0.36 °C	0.58 °C	0.91 °C	1.38 °C
12	0.33 °C	0.54 °C	0.88 °C	1.25 °C
13	0.28 °C	0.49 °C	0.77 °C	1.11 °C
14	0.25 °C	0.45 °C	0.70 °C	1.03 °C
15	0.20 °C	0.32 °C	0.65 °C	0.94 °C
16	0.18 °C	0.25 °C	0.58 °C	0.80 °C
17	0.22 °C	0.24 °C	0.47 °C	0.54 °C
18	0.14 °C	0.26 °C	0.44 °C	0.32 °C
19	0.18 °C	0.21 °C	0.28 °C	0.34 °C
20	0.25 °C	0.18 °C	0.30 °C	0.28 °C

Table 5.7: Maximum temperature deviation for the FBGs in water during self-heating evaluation

The tables show the maxima temperature deviations for each FBG in every test. As we can see, the FBGs closer to the irradiating tip can be easily individualized: they show the largest temperature shift in every test. FBGs that were further from the laser show narrower deviations.

In air, all the ΔT are below half a degree °C; with the laser on the range of variation increases with the increasing value of power. No linear relation can be found.

For what concerns the tests in water, since the stability test the range of variation is greater: also in this case it's possible to relate the increasing range of oscillations with the value of power.

Chapter 6

Creation of a Thermal Model

In this chapter a presentation of the **MATLAB® Partial Differential Equation Toolbox** (PDE) and its using for the creation of the liver thermal model is shown. Using this tool helped solving heat transfer equations both for the realization of a liver model and for the optimisation part.

In order to simplify the model of the liver, the geometry was considered two dimensional and not three; moreover, the tissue was considered as homogeneous. The formulation of the source of heating, corresponding to the effect of laser light interaction with the tissue has been obtained in two steps: first of all an equation that could express the optical interaction of laser during ablation has been found in a book, then a formulation that could express the heating source with the same sort of behaviour has been obtained combining different parameters.

6.1 MATLAB® PDE Toolbox

MATLAB® Partial Differential Equation Toolbox is an extension for MATLAB® that uses finite element method (FEM) in order to solve problems whose formulation is expressed with general partial differential equations (PDEs). In the first section a brief introduction of the tool is given, in the second a focus of the heat transfer problem.

6.1.1 Description of the Toolbox

There are many engineering applications for the tool: in general, it can solve linear and nonlinear second-order PDEs in stationary, time-dependent and eigenvalue problems using finite elements analysis.

Above the applications, the general workflow for solving a PDE or a system follows the same steps.

The first thing to do is to convert the equation in the form required by the tool. It can solve scalar equations expressed in the form:

$$m \frac{\partial^2 u}{\partial t^2} + d \frac{\partial u}{\partial t} - \nabla \cdot (c \nabla u) + au = f \quad (6.1)$$

otherwise eigenvalue equations expressed in the two forms: $-\nabla \cdot (c \nabla u) + au = \lambda du$ or $-\nabla \cdot (c \nabla u) + au = \lambda^2 mu$.

After, using the function `creatpde()` a model container is created: in the parenthesis the number of input arguments. Model container is an object containing all the informations about the model someone's developing.

The third step is to define the geometry: it can be 2 or 3 dimensional. The geometry can be defined in two ways: the first is to reconstruct the geometry from a *STF file* or mesh data, the second is to *create* the geometry with the toolbox functions. STF file is a very common extensions for most CAD software and to import the file the function `importGeometry`; in case of reconstructing the geometry for the mesh the function `geometryFromMesh` allows building a closed volume from the mesh. In case of creating the geometry the algorithm uses an approach called constructive solid geometry (CSG): it uses different simple solids (such as squares, circles...) to build a complex geometry. In case the geometry needed is 2-D there is also the chance to use **PDE Modeler app** that create geometries by drawing.

In both cases, the mesh of the imported or created geometry is divided in sub-domains where to evaluate PDEs solution with the command `generateMesh`: it can be triangular or tetrahedral. It is possible to plot the geometry and the mesh and see also numerical labels to edges and faces that correspond to the "name" of the specific geometrical component.

The next step is to specify coefficients and to set **boundary** and **initial** conditions. These can be applied to *edges* in case of a 2-D geometry otherwise to *faces* for 3-D. There are two kinds of boundary conditions for scalar PDEs:

- **Dirichlet Boundary Conditions:** it can be express with the equation

$$hu = r$$

u has to satisfy the equation on a face or an edge; h and r are function of the boundary of the domain, can be functions of space, time if the equation is time-dependent and also of the solution itself.

- **Neumann Boundary Conditions:** in the case of Neumann boundary conditions the solution u satisfies the equation:

$$\vec{n} \cdot (c\nabla u) + qu = g \quad (6.2)$$

where \vec{n} is the outward unit normal, q and g are functions of the boundary of the domain and can be function of space, time for time-dependent equations and of the solution.

In case of systems of PDEs the conditions will be the same number of the number of total input.

For time-dependent equations there is the possibility to set initial conditions of the transient.

Once all the features of the model are specified, PDEs can be solved using the appropriate solver: `solvepde` for scalar equations, `solvepdeeig` for eigenvalue problems. The solution can then be examined using a plot: there is also the chance to see the gradient plot.

6.1.2 Heat Transfer Problem

In the specific case of heat transfer problems, the toolbox solves "*conduction-dominant heat transfer problems with convection and radiation occurring at boundaries*" [29]

The characteristics of the material, the heat sources, the internal heat generation are all taken into account for the analysis of temperature distributions or heat fluxes.

In general, the workflow is the same that has been described in the previous section, though there are few differences.

Once created the thermal modal container, it has to be specified from the beginning if the problem has been considered for a steady-state or a transient. The partial differential equation for transient conduction is:

$$\rho C_P \frac{\partial T}{\partial t} - \nabla \cdot (k\nabla T) = f \quad (6.3)$$

where T is the temperature, C_P is the specific heat and f is the heat generated in the body.

In the model realized for this master thesis the coordinate transformations helped in solving parabolic 3-D equations reducing the problem to 2-D: the axisymmetric problem takes advantage of the rotation around the axis to reconstruct the volume. Considering a simple case of a cylindrical rod with internal heat source, initial temperature 0 and heat-transfer exchange at the outer boundary; the formulation of the problem is:

$$\rho C \frac{\partial u}{\partial t} - \nabla \cdot (k\nabla u) = q \quad (6.4)$$

where u is the temperature and q the heat generated.

ρ , C and k are the density, thermal capacity, and thermal conductivity of the material : these properties are assigned to the model while it is defined. They all depend on the material and can be specified with `thermalProperties`. When the geometry is complex, different properties can be assigned to different regions. In cylindrical coordinate system:

$$\rho C \frac{\partial u}{\partial t} - \frac{1}{r} \frac{\partial}{\partial \theta} \left(kr \frac{\partial u}{\partial \theta} \right) - \frac{1}{r^2} \frac{\partial}{\partial \theta} \left(k \frac{\partial u}{\partial \theta} \right) - \frac{\partial}{\partial z} \left(k \frac{\partial u}{\partial z} \right) = q \quad (6.5)$$

Since the problem is symmetric $\frac{\partial u}{\partial \theta} = 0$.

Now the equation has to be adapted to the form presented in 6.1:

$$\rho r C \frac{\partial u}{\partial t} - \frac{\partial}{\partial r} \left(kr \frac{\partial u}{\partial r} \right) - \frac{\partial}{\partial z} \left(kr \frac{\partial u}{\partial z} \right) = qr \quad (6.6)$$

and re-defining r and y as z and x axis:

$$\rho y C \frac{\partial u}{\partial t} - \nabla \cdot (ky \nabla u) = qy \quad (6.7)$$

If there is an internal heat source it is assigned to the object representing the model (`internalHeatSource`).

Boundary conditions can be distinguish in specific values of temperature at edges or faces, otherwise heat fluxes through. Either convective heat flux and radiating heat flux can be performed (`thermalBC`) is the function to apply boundary conditions). Both for steady-state and transient model an initial temperature or guess can be specified using `thermalIC`.

The last step is to solve and plot the results: it is possible to visualizes temperatures, temperature gradients, heat fluxes and heat rates.

Properties, boundary conditions and initial conditions can be also express with a function of time and space.

6.2 Model Realization

The realization of the liver model followed the flow-chart for heat transfer problems mentioned above. Few assumption were made:

- Tissue has been considered homogeneous;
- The liver is a 2-D section;
- No blood perfusion contribution was considered.

These simplifications should not affect the model for our application. Since the expression of the equation is adapted to MATLAB, x will refer to the radial direction and y to the axial.

6.2.1 Geometry and Thermal Conditions

The geometry realized is a simple rectangular: it represents a section on the cylinder whose geometry can be reconstruct with a rotation. In this way the symmetry of the cylinder has been exploited to study a planar geometry, but taking in account the original volume. For this reason the reference system is radial.

The dimensions were considered very small because the laser propagation in the tissue is less then few centimeters: the radius is 1 cm, while the height of the cylinder is 2 cm. Fig. 6.1 This choice has also been made to reduce the space of

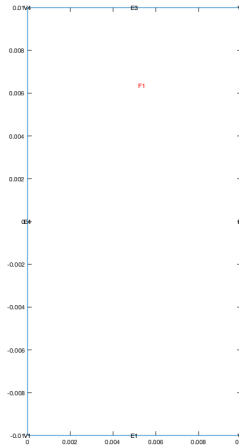


Figure 6.1: Geometry used for the model. The origin is in the middle of the right edge and that is where the tip of the laser has been put.

investigation of the algorithm: the *mesh* generated has a very narrow dimension of 0.09 mm, thus it slows down solving the PDEs in each region. (Fig. 6.2)

The thermal properties assigned to the tissue depends also on the position; they have been assigned with this formulation:

- Thermal conductivity :

$$k = 0.57 \cdot x; (W/(mK)) \quad (6.8)$$

- Specific heat:

$$c = 3500 \cdot x; (J/(kgK)) \quad (6.9)$$

- Mass density: $\rho = 1070$ (kg/m³)

As was already said, the density is constant for the homogeneous material hypothesis.

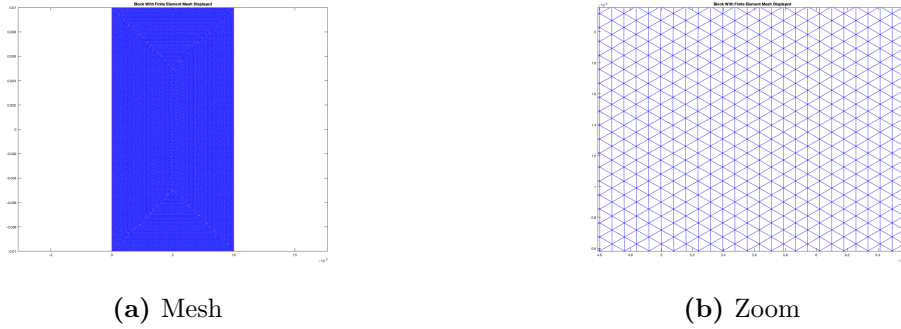


Figure 6.2: a) Mesh realized using the function `createMesh`. The maximum value of edge is 0.09mm. b) Zoom to have a better perception of the triangulation.

The optical parameters are used to simulate the two causes of absorption: *attenuation* and *scattering*:

- $\mu_a = 76 \text{ m}^{-1}$ attenuation coefficient;
- $g = 0.9$ degree of anisotropy. This value considers the optical path difference of photons in the tissue due to scattering phenomenon. It is dimensionless;
- $\mu_s = 10015 \left(\frac{1}{\text{m}}\right)$: this is the scattering coefficient in each medium;
- μ_{eff} : the effective attenuation coefficient measure the effect of scattering and absorption due to diffusion approximation. [30]

$$\mu_{\text{eff}} = \sqrt{3\mu_a(\mu_a + \mu_s(1 - g))} \quad (6.10)$$

Optical parameters were found in a previous Master Thesis Work applying the Montecarlo Method through the software Monte Carlo Multi Layered (MCML) and then a second software named Convolution (CONV). The first one (MCML) simulates the photons distribution in a portion of a cylinder: in the program, the infinitesimal light beam hit perpendicularly the volume and then analyze for the portion several optical parameters. Moreover, CONV applies a spatial convolution to convert the impulsive light beam to a real case by fixing several parameters. [31] For what concerns the boundary conditions both Dirichlet and Neumann have been adopted: the temperature of the borders of the tissue are considered at the constant temperature of 25 °C since they are too far from the source to be affected by the laser. This is a Dirichlet condition. For the radial geometry, the axis of rotation -where the optical fibre is partially positioned- has an heat flux equal to 0. All the system starts the transient at the temperature of 25 °C because it was generally the temperature of the room where the test took place.

6.2.2 Modelization of liver ablation

Heat source is represented by a laser light beam irradiated by a multi-modal optical fibre: this effect has been modeled as an internal heat source for the positioning of the fibre inside the geometry. The value of power can be set: the values used in the model were chosen according to the experiments *ex-vivo* on the liver (0.5, 1, 1.5 and 2 W). [32]

The shape of the beam determines the expression of the internal heat source:

- for a Gaussian shape:

$$q(r, z) = \begin{cases} \mu_a \frac{2P}{\sigma^2 \pi} e^{(-\alpha_{\text{eff}} x \cdot y)} e^{\frac{2x^2}{\sigma^2}} & z \geq 0 \\ 0 & z < 0 \end{cases} \quad (6.11)$$

- for a rectangular window:

$$q(r, z) = \begin{cases} \mu_a \frac{P}{\sigma^2 \pi} e^{(-\alpha_{\text{eff}} x \cdot y)} \cdot \text{rectwin}(r, z) & z \geq 0 \\ 0 & z < 0 \end{cases} \quad (6.12)$$

where *rectwin* is the rectangular window, defined as follow:

$$\text{rectwin}(r, z) = \begin{cases} 1 & |r| \leq \sigma \\ 0 & |r| > \sigma \end{cases} \quad (6.13)$$

In both formulas the factor σ takes in account the effect of the numerical opening of the optical fibre, defined as:

$$\sigma = \sigma_0 + \tan(\theta) \cdot y \quad (6.14)$$

for the Gaussian-shaped beam σ_0 is one third the core radius, for the rectangular window is equal to the radius. $\theta = \arcsin \frac{0.22}{n}$, where $n = 1.33$ is the refractive index of water, that is the main component of the tissue.

In the formulation of the heat source both shapes have a part defined by an exponential decay on radial and axial direction, what changes is in the radial direction where two different geometries modulates the output.

Another difference is a "2" factors in the first part of the equation: it has been demonstrated that, to achieve a same value of energy in the two cases, the peak power has to be scaled. The intensity of a Gaussian beam:

$$I(\rho) = I_0 e^{-\frac{2\rho^2}{\omega_0^2}} \quad (6.15)$$

$$\begin{aligned} P &= \frac{1}{2} Y \int_{\Sigma} I(\rho) d\Sigma = \frac{1}{2} Y I_0 \int_0^{2\pi} d\phi \int_0^{\infty} \rho e^{-\frac{2\rho^2}{\omega_0^2}} d\rho \\ &= \frac{1}{2} Y I_0 2\pi \left[-\frac{\omega_0^2}{4} e^{-\frac{2\rho^2}{\omega_0^2}} \right] = \frac{\omega_0^2}{4} Y I_0 \pi \end{aligned} \quad (6.16)$$

Therefor the intensity is:

$$I_0 = \frac{4P_0 Z_0}{n\pi\omega_0^2} \quad (6.17)$$

where $Z_0 = \frac{n}{Y}$ and it is the impedance in the vacuum. For the rectangular window:

$$I(\rho) = I_0 p(\rho) \quad (6.18)$$

where $p(\rho)$ is the window.

$$\begin{aligned} P &= \frac{1}{2} Y \int_{\Sigma} I(\rho) d\Sigma = \frac{1}{2} Y I_0 \int_0^{2\pi} d\phi \int_0^{\omega_0} \rho d\rho \\ &= \frac{\omega_0^2}{2} Y I_0 \pi \end{aligned} \quad (6.19)$$

$$I_0 = \frac{2P_0 Z_0}{n\pi\omega_0^2} \quad (6.20)$$

When all the variables are defined it is possible to solve the equations: as the model is transient, each simulation consider the laser irradiating for 3 minutes, and equations are solved considering a step of 1 s.

In 6.3 and 6.4 the shape of the beam is represented. As was previously demonstrated the peak value for the Gaussian distribution is the double respect to the rectangular window. The Gaussian curve has a faster descend and all the power is focused on the top; on the contrary the rectangular window has a slower descend therefor power is distributed on a major area.

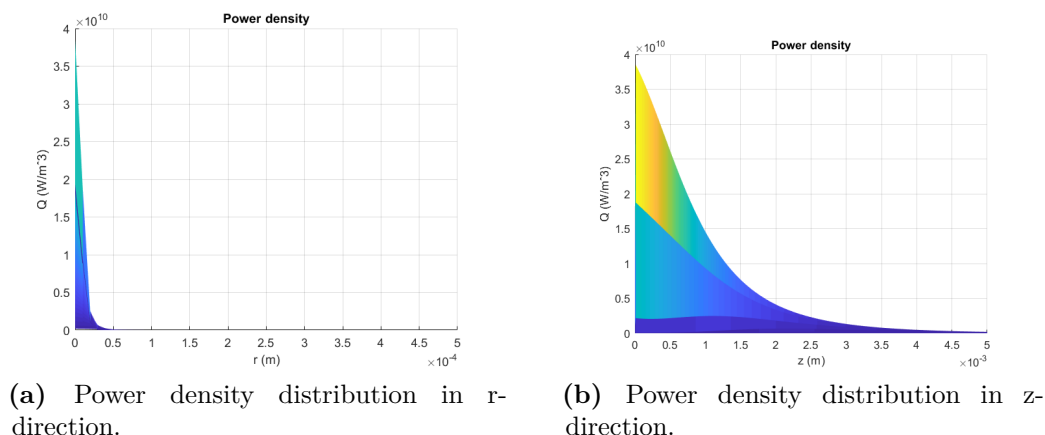


Figure 6.3: Power density distributions for the Gaussian model.

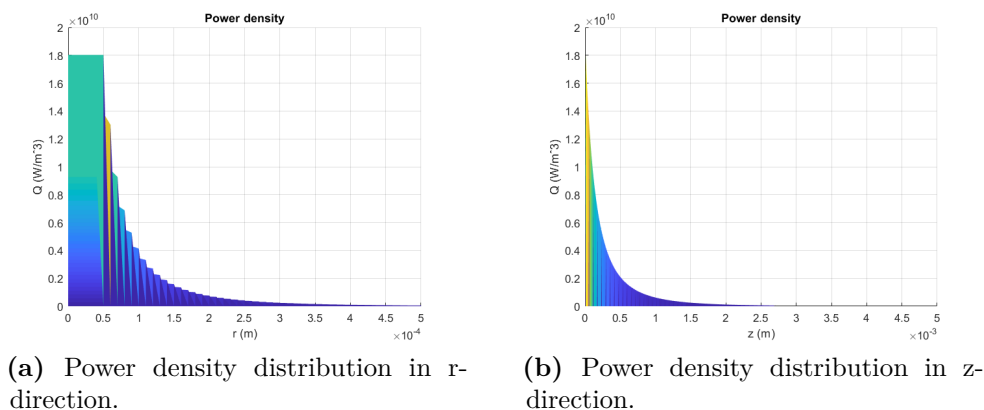


Figure 6.4: Power density distributions for the rectangular model.

6.2.3 Results and Conclusions

Below results are presented. For each power value model with the "Gaussian-shaped" beam and the rectangular window are compared. For each plot, on the left there is the heat map with the temperature bar beside showing temperature distribution at the end of the transient for a point closer to the laser tip. On the right there is the temperature trend for four different coordinates. The trend is the same, what changes are the temperatures reached during the transient.

From the pictures is clearly visible that, for each power value, temperatures are higher for the rectangular window model. Moreover, the area where temperatures are higher is wider for the former. During the *ex-vivo* ablation performed a multi-mode delivery fibre was used and we think that the rectangular window would

better modelize the fibre.

These consideration led to the choice of using the rectangular window shaped beam since its behaviour is more similar to the reality, especially compared to the trials done with the liver.

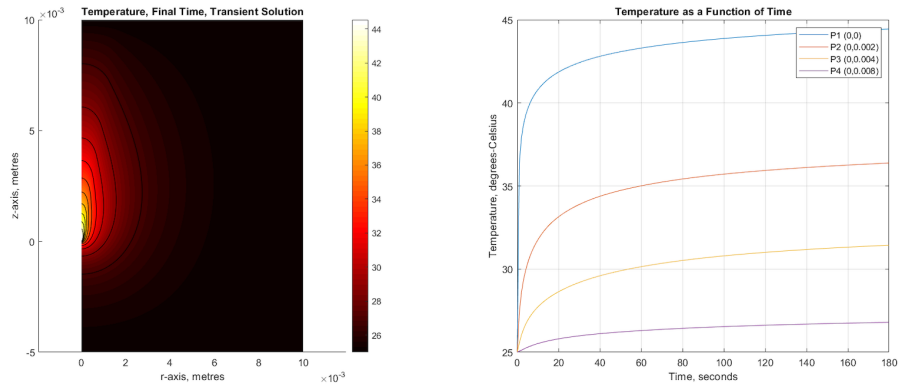


Figure 6.5: Temperature distribution and trends for the rectangular window. Power set at 0.5 W.

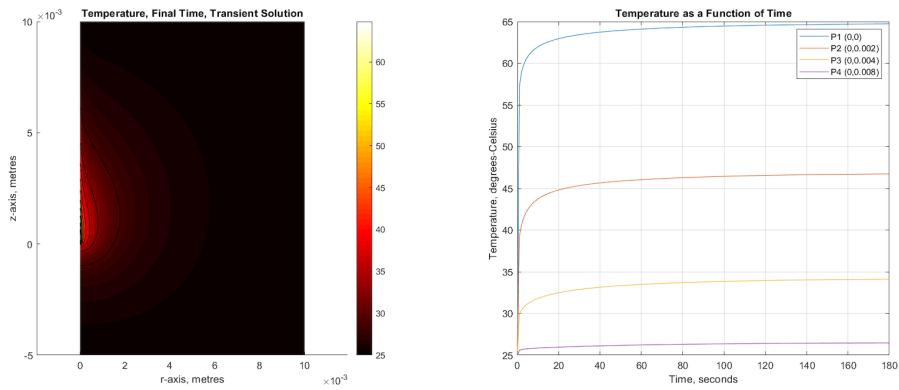


Figure 6.6: Temperature distribution and trends for the Gaussian window. Power set at 0.5 W.

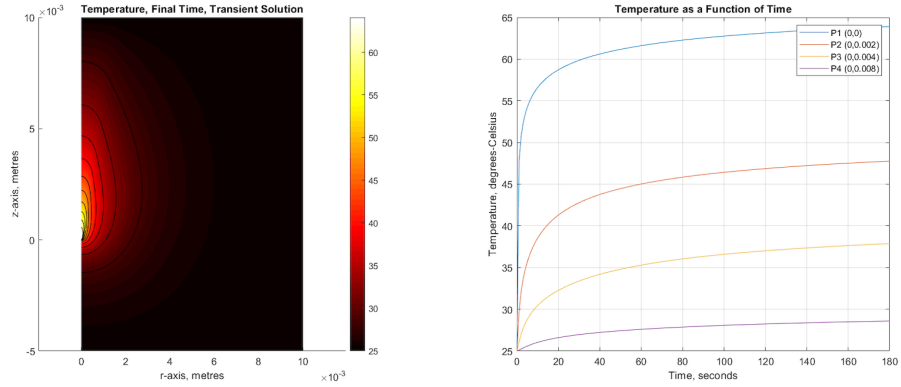


Figure 6.7: Temperature distributions and trends for the rectangular window. Power set at 1 W.

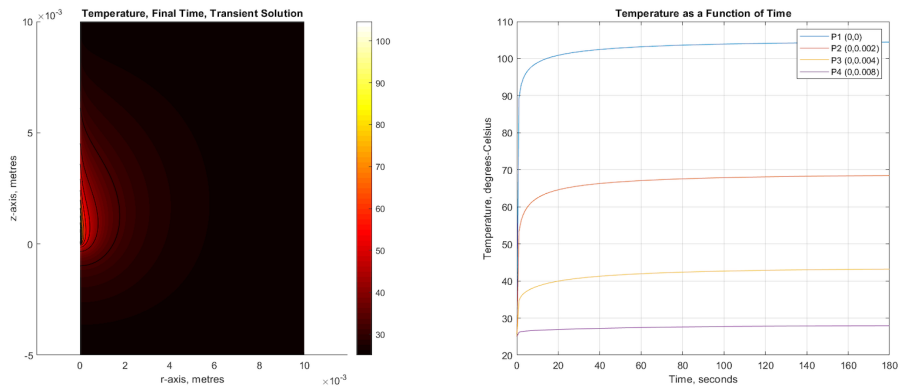


Figure 6.8: Temperature distribution and trends for the Gaussian window. Power set at 1 W.

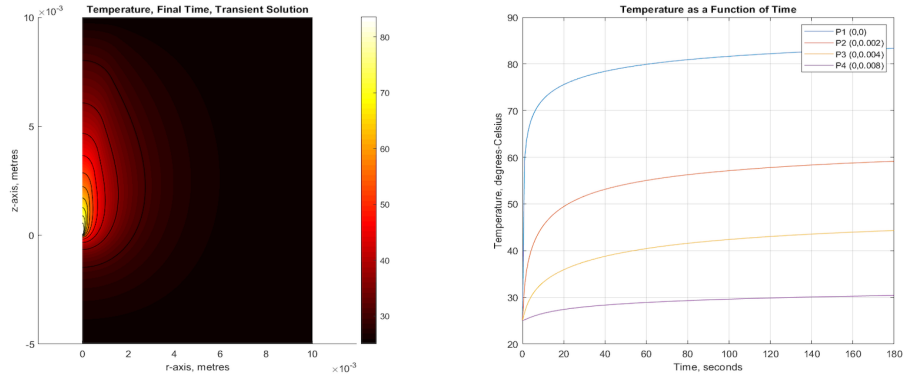


Figure 6.9: Temperature distributions and trends for the rectangular window. Power set at 1.5 W.

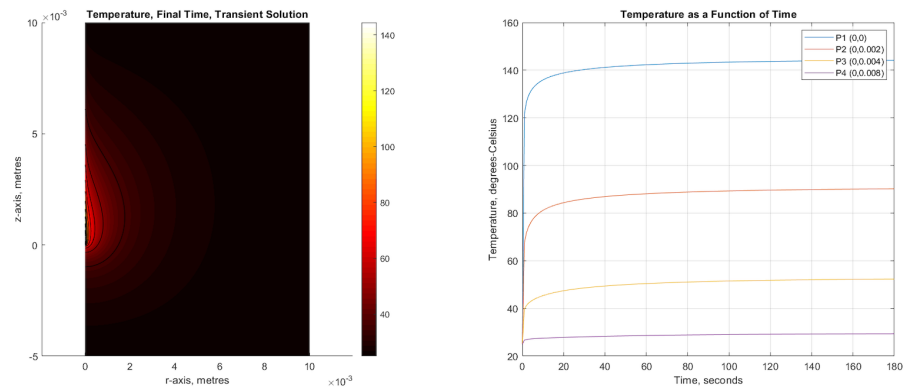


Figure 6.10: Temperature distribution and trends for the Gaussian. Power set at 1.5 W.

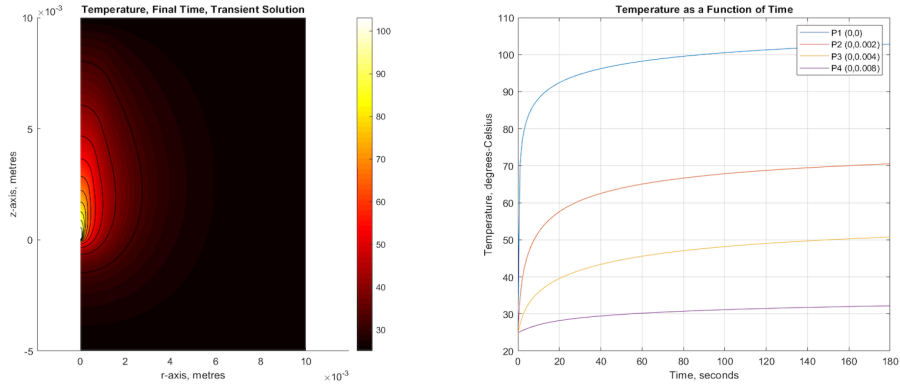


Figure 6.11: Temperature distributions and trends for the rectangular window. Power set at 2 W.

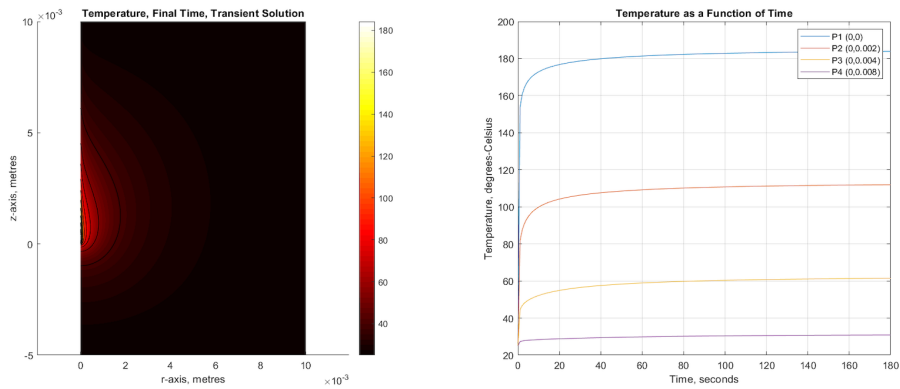


Figure 6.12: Temperature distribution and trends for the Gaussian. Power set at 2 W.

Chapter 7

Ex-vivo Liver Ablation

In order to achieve an optimization of liver parameters *ex-vivo* bovine liver ablation was performed. In the trials quasi-distributed temperature sensors (FBGs) were used for measuring temperatures during the laser ablation, performed at different power values. There are two reasons why different values have been tested: the first is linked to the possibility of breaking sensing optical fibres when high temperatures are reached and the second is to have a larger data set for the optimization. Although FBGs are quite resistant, we performed fibre thinning due to the melting of the cladding made in polymethylmethacrylate caused the increasing temperature. This phenomenon occurred several times when the power was set at 2 W. Then, these samples have been compared to model previsions for the same supply of power.

7.1 Set up and Measurements

To perform *ex-vivo* liver ablation the instrumentation needed is simple. Some of the instruments needed in the test have already been explained in previous sections. The instruments are:

- **Optical Interrogator MicronOptics HYPERION Si155:** only three channels have been used. The sampling rate was set at 2/5 Hz;
- **Laser Unit:** the laser used in the tests has been realized in another Master Thesis work. [33]. Technical implementations have been chosen considering the field of application of the laser, therefore biomedical. Some relevant characteristics are:
 - **Laser Diode:** the type is BMU9-9xx-01/02 R realized by II-VI. It is an *uncooled multimode laser diode module*. From data sheet, the features are:

- * High output power: 9W
- * 105 μm core 0.15 or 0.22 NA multimode optical fibre: 0.22 NA has been used;
- * Hermetically sealed 2-pin package;
- * Floating anode/cathode;
- * High reliability;
- * Excellent solderability;
- * Standard wavelengths: at 915,940,960 and 975 nm. We used 915 nm;
- * RoHS compliant.

The maximum value for the optical power was measured and it is 7W and the threshold current is 0.5A: below this value of current there is no emission. The maximum value of current is 8.5 A with a tension of 1.9 V. Its wallplug efficiency -the ratio between the output optical power and the input electrical power- is around 48 %. In Fig. 7.1 the calibration curve is reported. The wavelength of the emitted beam is 915 nm;

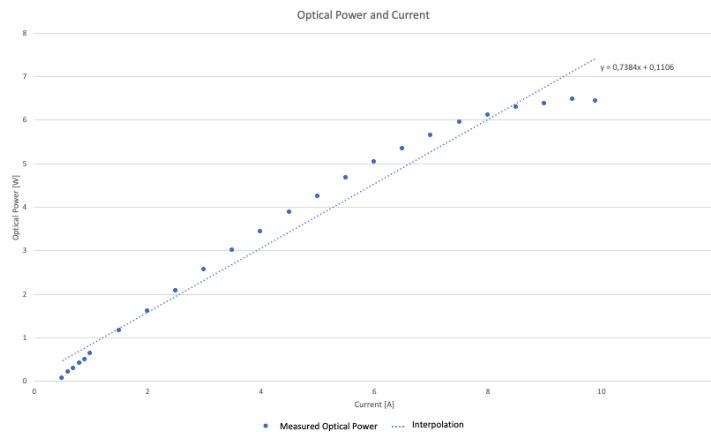


Figure 7.1: Data interpolation: calibration of the diode.

- **Double Operating Mode:** the emission can be continuous (CW) or pulsed (PW);
- **Output Connector SMA905:** the delivery optical fibre here is connected;
- **Electronic Clock:** there is a Real Time Clock (RTC) that helps setting the timer as well;
- **Controller:** to manage the laser parameters;
- **User Interface:** to set laser parameters (wavelength, power, operating mode);



Figure 7.2: Complete Laser Unit. The keypad is used to insert the password, the power, the timer. When pushed, the red button below the display send the information of starting the emission. There is an emergency stop, a safety key and LEDs that help understanding laser status.

- **Three Photosensitive Single Mode Fiber** : each fibre was used to measure tissue temperatures. They were characterized in 5, Chapter 1 of the Experimental Part. Some features are:
 - Enhanced Photosensitivity;
 - Low Loss Photosensitive Fibers;
 - Cladding Mode Suppressed;
 - Select Cut-Off Photosensitive Fibers;
 - Dual Acrylate coating
- **One multi-mode optical fibre:** to delivery the laser light on the tissue. It was connected to the diode using a SMA-905 connector;
- **Caliber:** it was used to measure the distances between the different fibres;
- **Two liver slices:** in the trials a "*sandwich*" configuration was used.

All the instruments have to be turned on: it is a good practice to turn up the MicronOptics and the Laser unit quite before the using to let the instrumentation stabilize.

Each fibre has been connected as follow:

1. the straight array is connected to channel 1 of the MicronOptics;
2. the ultradense array positioned in the same direction as the delivery optical fibre is connected to channel 2;
3. another ultradense array is positioned 1mm to the right respect to the former ultradense array.

The delivery fibre is connected to the laser unit. Meanwhile, the optical fibres are places on the liver as pictured in Fig. 7.3: a caliber was used to make sure distances agreed with the scheme. It was important to keep relative distances during all the tests: in the model the same distances were analysed to find temperature distribution.

After making sure the positioning of the fibres is the same as in the picture, the second slice of liver covered the whole setup. We chose not to use a single thicker slice because it would be too difficult to maintain arrays positioning without the help of the caliber. The pressure of the second slice guarantees the contact of the four optical fibres with both upper and lower tissues. The "sandwich" helps simulating inserting of the laser inside the tissue.

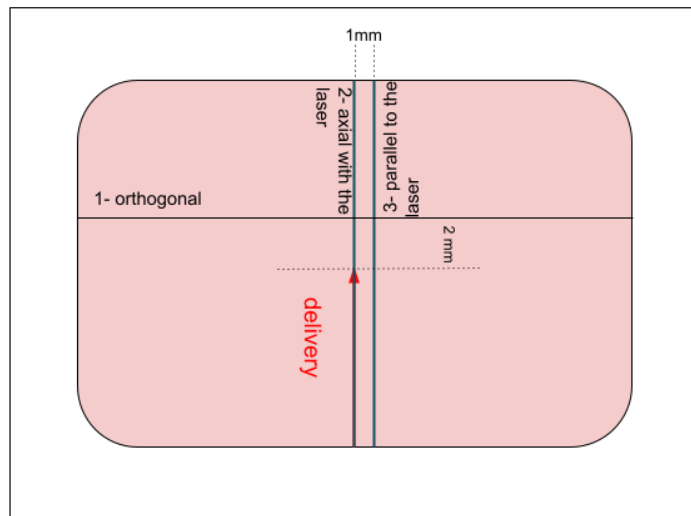


Figure 7.3: Simple scheme of how optical fibres have been placed on the lower liver slice.



Figure 7.4: Real setup used for the trials. After each value of power all the gratings were moved in order not to affect the next results.



Figure 7.5: Zoom of the setup with the caliber.

Next, laser parameters can be set up using the **User interface** as the following pictures show:

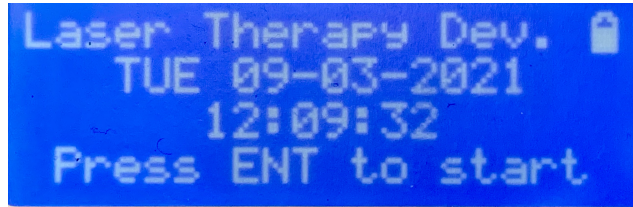
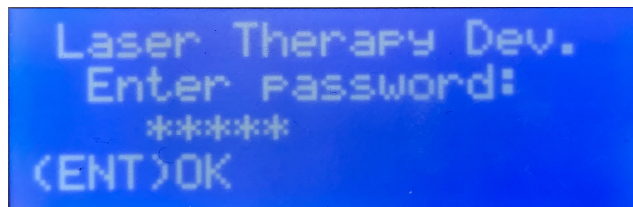
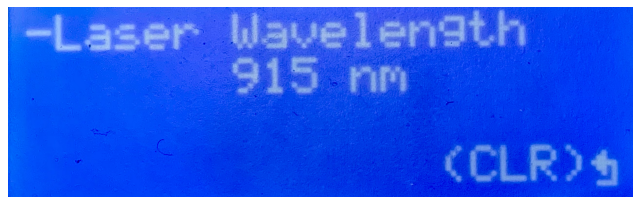


Figure 7.6: Display when the device is turned on.

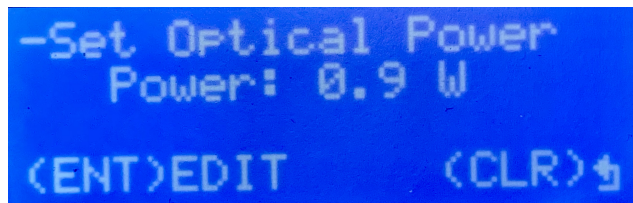
A password is requested to access settings for the laser: this is compulsory for the class of the device. It is a 5 digits code.



Choice of wavelength: the device has a diode that emits at 915nm;



Through a keypad the power is chosen. Although an optical power is asked, at the moment the device works setting the equivalent current. In 7.1 values that have been used are shown.



Current(A)	Power(W)
0,9	0,483
1,204	1
1,881	1.5
2,559	2

Table 7.1: Current used to set the laser and its equivalent power value.

Operating Mode: there is the double chance to work in continuous or pulsed wave. For the pulsed wave mode frequency and duty-cycle must be set.

```
-Select Mode
  Laser Mode: CW
<ENT>PW      <CLR>↓
```

```
-PW Mode Settings
Freq: 5 Hz  DC: 50 %
<ENT>EDIT    <CLR>↓
```

There is also the possibility to set a timer for laser light emission:

```
-Set Timer Count
  Timer: 03:00
<ENT>EDIT    <CLR>↓
```

Then, the user is asked to confirm settings:

```
-Ready?
Press ENT to confirm
  laser setup
<ENT>OK      <CLR>↓
```

Another security precaution, that is also compulsory for the class of the device, is a key. When the key is on the "0" the laser beam cannot be emitted: only turning the key to "1" is possible starting the emission. A pushing button is actually what starts irradiation.

For the MicronOptics a sampling frequency of 5Hz was used. Generally, each recording started few minutes before the laser was actually emitting and was stop later then the laser finished. This has been done to see tissue temperature distribution before and after heating.

7.2 Results and Conclusion

Signals acquired have been elaborated in MATLAB® to obtain temperature arrays used for the optimization. Data from the MicronOptics are filtered in the same way as for the characterization: the number of samples to average was evaluated plotting the signals and considering the largest number possible not to compromise the information. For the lowest value of power (0.5 W) no visible effect was seen on the tissue. This is understandable since temperatures reached during these tests are not high enough.

In 1, 1.5 and 2 W cases, effects were visible eventually on both slices of the liver: of course the dimension of the sign increases with the increasing power.

During the day, different tests at the same power value were done: we could see temperatures changing changing positioning of the fibres, for the same power. Furthermore, the variability increases changing the liver. We address first changes to tissue water loss and air exposure; differences between several livers were also visible. For instance, some slices has a major blood component, which means a major water content too and this influences tissue reaction therefor also thermal conductivity.

The dimension of the wound increases with the increasing power. As well as for the model, the highest temperature is not reached where the laser tip is, but a little further.

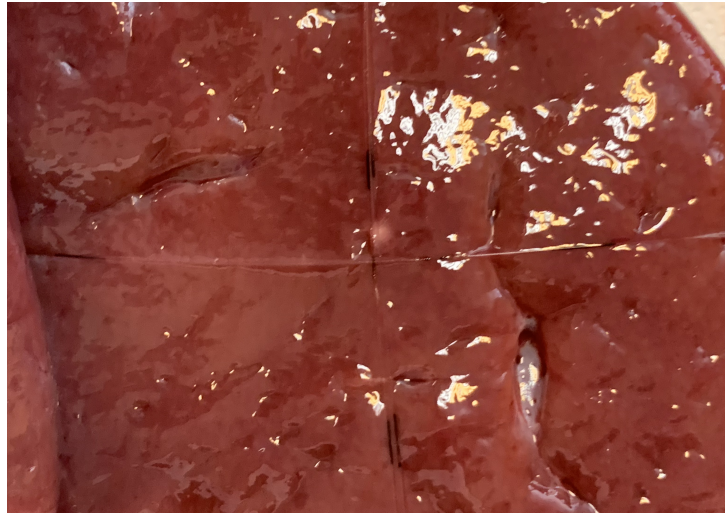


Figure 7.7: Liver after 180 s ablation with power 1 W.

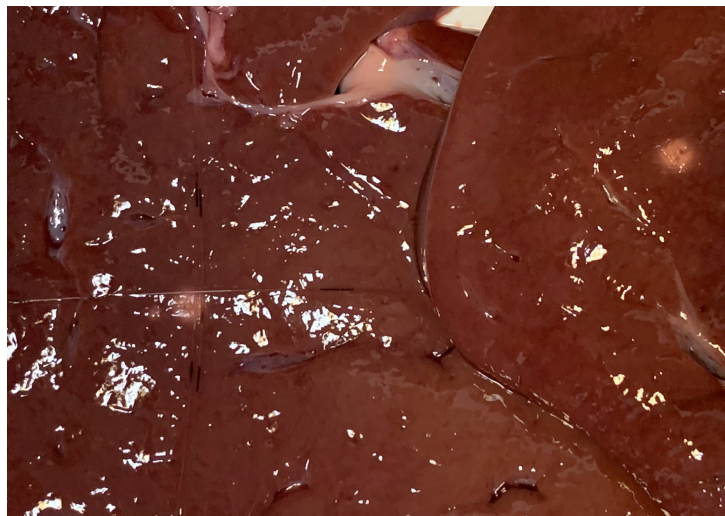


Figure 7.8: Liver after 180 s ablation with power 1.5 W. On the right there is the lower slice where the laser was lean on, on the right there is the upper slice where we can see the effect of ablation anyway.

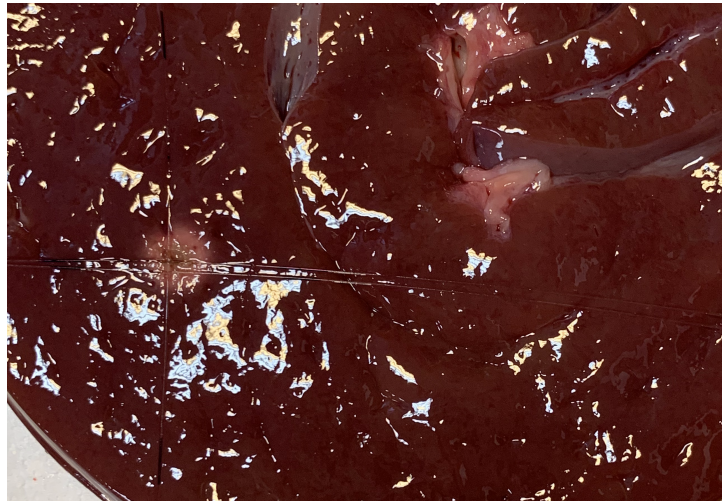


Figure 7.9: Liver after 180 s ablation with power 2 W.

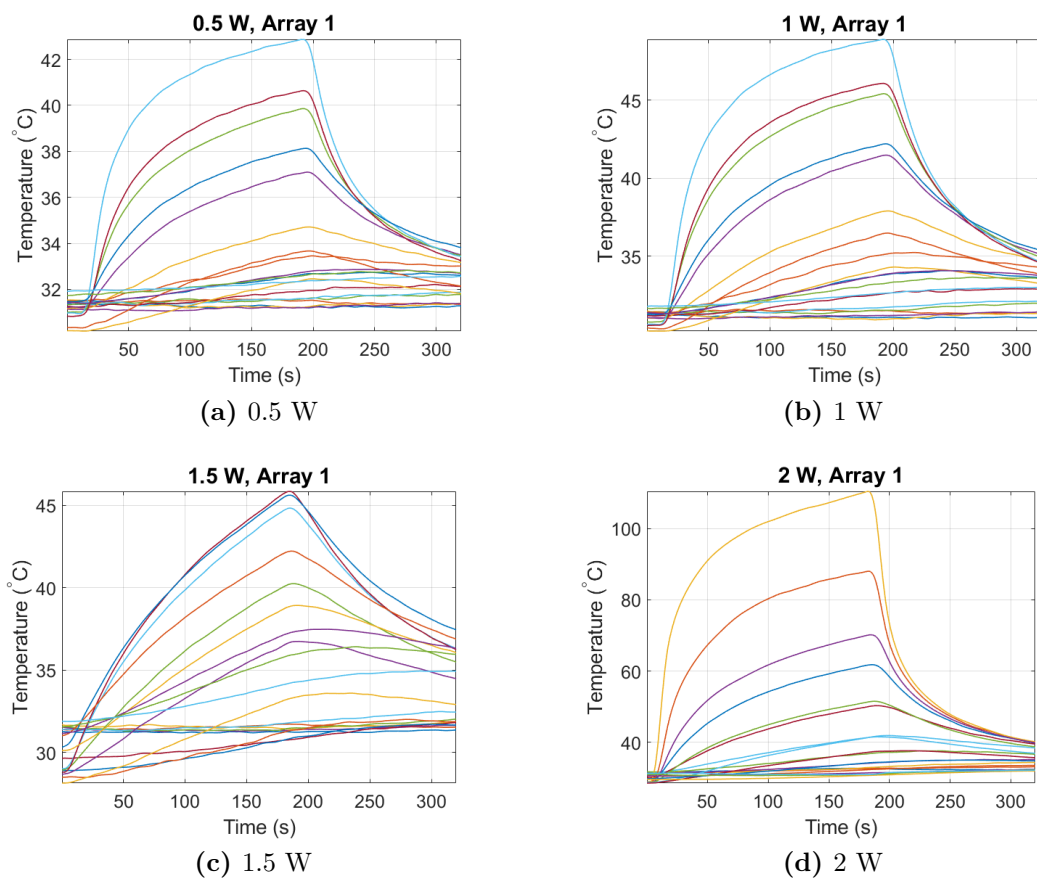


Figure 7.10: Temperature trend during ablation for Array 1. 7.3

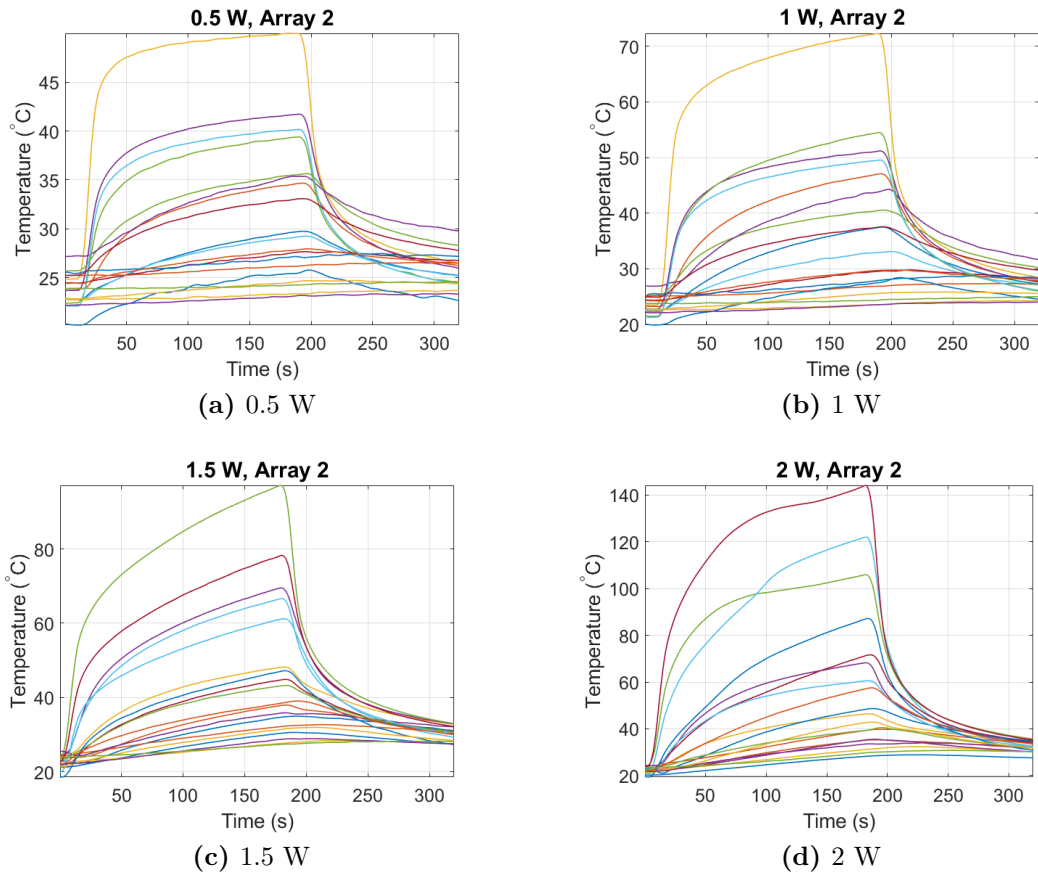


Figure 7.11: Temperature trend during ablation for Array 2. 7.3

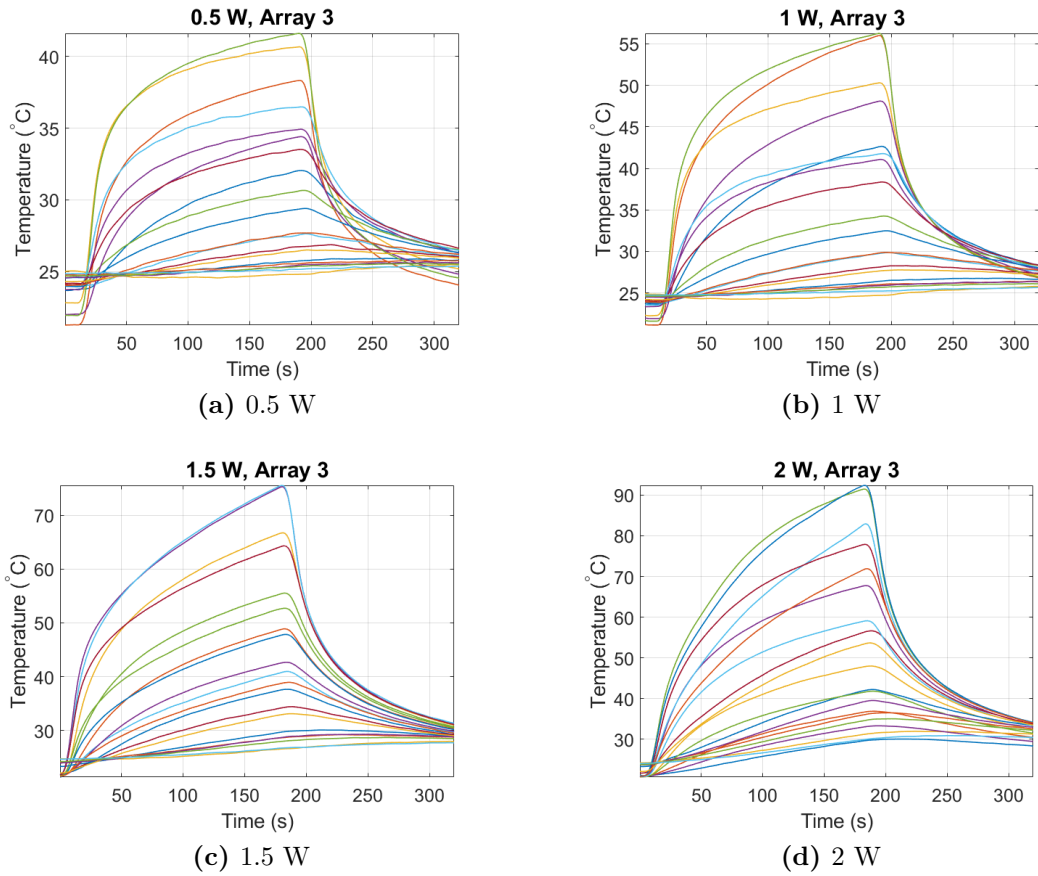
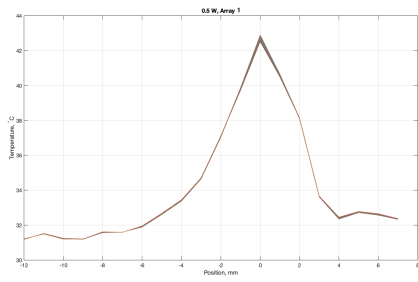
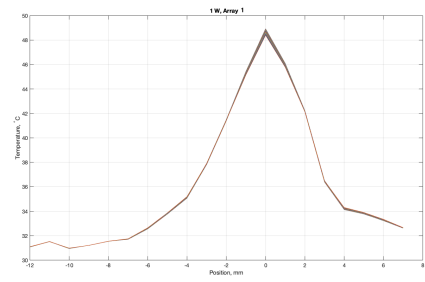


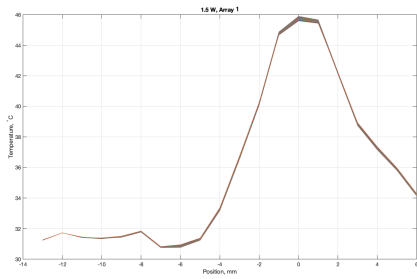
Figure 7.12: Temperature trend 5 s before and 5 s after ablation for Array 3. 7.3



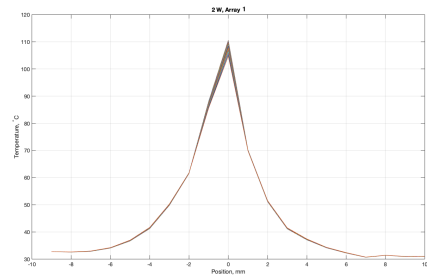
(a) 0.5 W



(b) 1 W

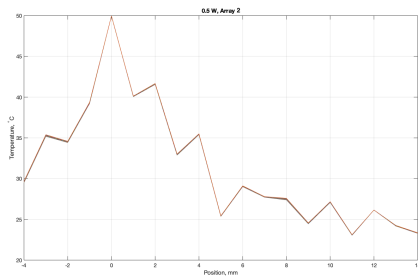


(c) 1.5 W

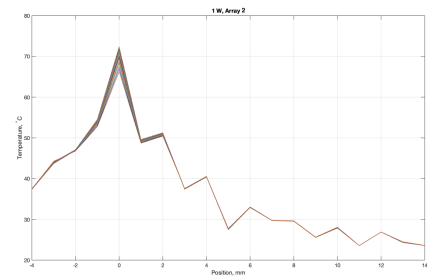


(d) 2 W

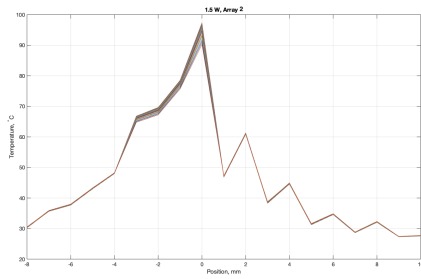
Figure 7.13: Temperature trend 5 s before and 5 s after ablation respect to the position for Array 1. 7.3



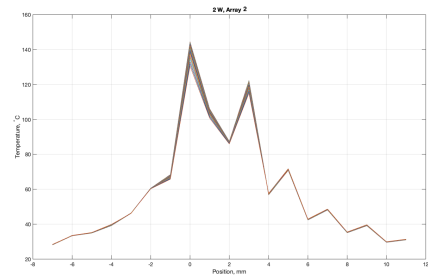
(a) 0.5 W



(b) 1 W

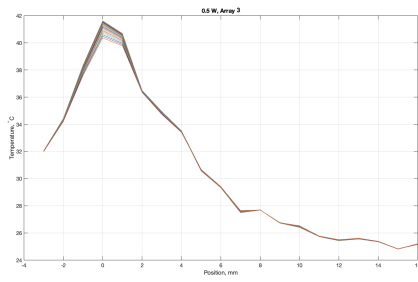


(c) 1.5 W

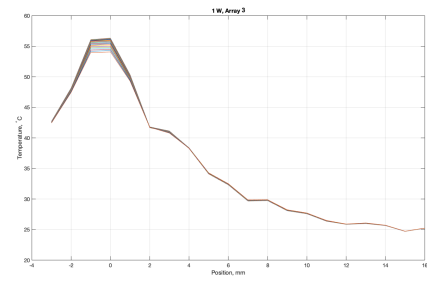


(d) 2 W

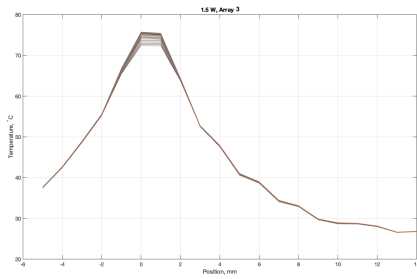
Figure 7.14: Temperature trend 5 s before and 5 s after ablation respect to the position for Array 2.



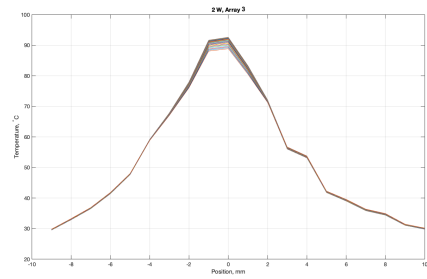
(a) 0.5 W



(b) 1 W



(c) 1.5 W



(d) 2 W

Figure 7.15: Temperature trend 5 s before and 5 s after ablation respect to the position for Array 3. 7.3

Chapter 8

Optimization

In this chapter optimization results are presented.

Although in literature liver optical and thermal parameters can be found, mostly they change with the changing of the method that led to the estimation as well. For this reason in this work we have tried to achieve a coherent estimation with the purpose: laser ablation.

The realization of the model helped understand the best expression for the heat source compared to results obtained in real *ex-vivo* ablation; here we try to find a value for parameters that fits the best the real case. These parameters are:

- **k thermal conductivity;**
- **α attenuation coefficient;**
- **α_{eff} scattering coefficient**

For these work it has not been considered the influence of temperature on the parameters, but in reality they change with the temperature with a different behaviour according to the temperature reached.

8.1 Algorithm principles

The algorithm is made of one main program and two functions that are "called" by the main. In the main program the array of temperature distribution is extracted from the recording of the three minute *ex-vivo* ablation for the confrontation of the estimation made by the model.

It starts with the loading of the text file recorded during the ablation from the MicronOptics; the peaks are filtered with a FIR filter on 10 samples in order to reduce the noise effect on calculating the temperature. The formula used for

temperature is the inverse of 4.2, so:

$$T = \frac{\lambda_B - \lambda_0}{k} \quad (8.1)$$

The only array used in the model is the one on the same axis as the delivery fibre: it is an ultradense array, therefore temperature have been organized in order to assign the correct position in the array to the corresponding position on the optical fibre. After finding the highest temperature reached during the ablation - which is associated to the FBG closest to the laser tip - the array is reduced from 20 to 10 elements. The temperature abovementioned occupies position one; the following 9 values are the remaining elements of the array.

In this way each temperature in one millimeter further from the previous and we obtain the temperatures spatial distribution to compare to the model.

The next step is starting the optimization, which has several steps. It is part of the main program as well, but "calls" a different function (called "*difference*") that actually finds the difference between the temperature measured and the evaluated temperature by the model, that "*difference*" itself calls.

The model works as well as the one described previously, with the diversity that the parameters that have to be optimize are unknowns. Temperature starts to be calculated from the parameters used in the model described in the previous chapter and then they are optimize. The range of variability of the parameters is set in order to avoid values that would not be reasonable considering the biological tissue. The proper optimization employs the function `fminsearch` that "*find minimum of unconstrained multivariable function using derivative-free method*". It is a non linear solver that search to minimize the function specified by the user, therefore the inputs are:

- **the function to minimize:** in our case it is the difference between the temperatures;
- **starting points:** we used the values of the chapter of realizing the model;
- **optimization options:** specified using `optimset`. In the specific case, it has been used to specified a maximum number of function evaluations('MaxFunEvals') to 1000.

The output is a three elements array that contains the optimized thermal conductivity k , attenuation coefficient α and scattering parameter α_{eff} .

8.2 Results

For each power value parameters have been evaluated considering only the temperature of the axial array. Analyzing the different results we were able to find out

the best parameters to fit temperatures.
They have been found for each power value.

	k (W m ⁻¹ K ⁻¹)	μ_a (m ⁻¹)	μ_s (m ⁻¹)
0.5 W	0.200	23.375	7752.637
1 W	0.800	59.245	9122.201
1.5 W	0.799	59.140	12999.997
2 W	0.200	17.020	9868.310

Table 8.1: Values of the parameters optimized.

In 8.2, 8.3, 8.4 and 8.5 the difference between the measured temperature and the calculated with the model using the parameters of optimization are presented.

	FBG1	FBG2	FBG3	FBG4	FBG5
$\Delta T(^{\circ}C)$	0.403	0.406	0.384	0.127	0.097
	FBG6	FBG7	FBG8	FBG8	FBG10
$\Delta T(^{\circ}C)$	0.214	0.235	0.210	0.191	0.184

Table 8.2: Temperature variation between the calculated and the evaluated temperature during the trials at 0.5 W.

	FBG1	FBG2	FBG3	FBG4	FBG5
$\Delta T(^{\circ}C)$	1.291	1.057	1.022	1.650	0.268
	FBG6	FBG7	FBG8	FBG8	FBG10
$\Delta T(^{\circ}C)$	1.072	2.171	2.656	2.098	0.219

Table 8.3: Temperature variation between the calculated and the evaluated temperature during the trials at 1 W.

	FBG1	FBG2	FBG3	FBG4	FBG5
$\Delta T(^{\circ}\text{C})$	1.899	1.804	2.161	2.869	0.604
	FBG6	FBG7	FBG8	FBG8	FBG10
$\Delta T(^{\circ}\text{C})$	2.021	4.466	5.848	5.114	1.242

Table 8.4: Temperature variation between the calculated and the evaluated temperature during the trials at 1.5 W.

	FBG1	FBG2	FBG3	FBG4	FBG5
$\Delta T(^{\circ}\text{C})$	0.256	0.727	1.685	1.778	0.223
	FBG6	FBG7	FBG8	FBG8	FBG10
$\Delta T(^{\circ}\text{C})$	0.646	0.143	0.841	1.267	3.015

Table 8.5: Temperature variation between the calculated and the evaluated temperature during the trials at 2 W.

The lowest value of power, the lowest error, though there is no obvious relationship between the power used and the error estimated.

We can also observe that the biggest error is for the same value of power used for the estimation of the parameters: in Fig. 7.14 we can see an unexpected peak of temperature that may have caused bias for that FBG.

Another factor to take in account when analyzing the error is the several number of hypothesis made *a priori*. The temperature actually influences the changing of parameters since tissue composition change as well. This was not taken in account in the model, as well as for the effect of cavities on the slice close to the laser or the sensor.

Furthermore, above the precautions, the upper slice may have influenced the data acquisition due to the introduction of strain as well.

The parameters are found for *ex-vivo* ablation: during *in-vivo* ablation things are quite more complicated because there are also more factors to take in account such as metabolic heat transfer, vessels effect, percentage of water content in the tissue and the effect of changing tissue properties on the laser delivery fibre as well.

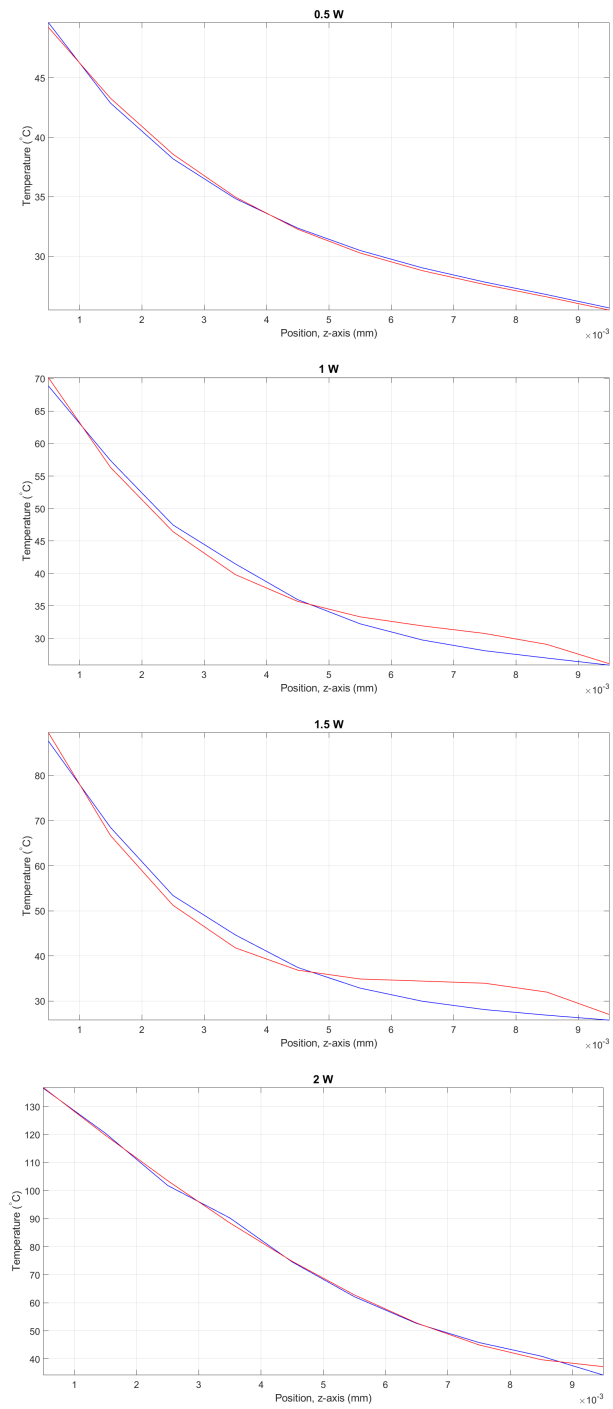


Figure 8.1: Comparison of the trend of the measured temperature and the one evaluated using optimization parameters. In red there are the measured ones and in blue the evaluated.

Chapter 9

Conclusions

In this Master Thesis work the focus has been on the use of laser during cancer ablation, performed *ex-vivo* on hepatic tissue in the trials. The aim was to optimize parameters such as thermal conductivity, attenuation and scattering factors to obtain a liver model whose temperature distribution fits the real one.

Since there is the need to measure temperatures the first step was characterizing the fibre Bragg gratings: they are optical fibre sensors generally used for their good thermal and stress resistance. FBGs are structures realized changing periodically the refractive index along the core: when interaction with laser occurs, the FBGs behave like a notch filter and the reflected light is at a specific wavelength called Bragg wavelength. Each grating is associated to a specific wavelength and by the shift of this parameters it is possible to measure different physical quantity such as temperature or strain. The Bragg wavelength is linked to temperature with a linear relationship which would ease the evaluation, though strain has the same effect on strain and it is hard to distinguish the two effects.

For our work two kind of FBGs have been adopted: straight along the core and ultradense. The former has less spatial resolution and have been used for measuring temperature orthogonally respect to the laser light. The latter has a major resolution since FBGs are placed on two parallel lines respect to the core and we have used two of them to measure temperature along the axis of the laser and parallel.

In order to measure the wavelength shift Micron Optics HYPERION si155 have been used: it is an interrogator with tuneable laser that acquires the reflected optical power coming from the "written" fibre connected to one channel and convert it in voltage.

To characterize the gratings also a Thermocouple J-type has been used to associate the wavelength to a temperature measure: in this way characteristics parameters such as λ_0 and k have been found.

The next step has been creating a thermal model that could be representative for

liver ablation. It has been used MATLAB[®], specifically the Partial Differential Equation toolbox. The toolbox allows to solve the heat transfer model to a certain geometry that can be either created or imported. We used a 2-D geometry to simplify the problem and relieve the computational burden. It was considered with a radial reference system since it represents a slice of the cylinder that is obtained by the rotation across the principal axis.

Properties are assigned to the tissue as thermal conductivity, specific heat and mass density, which is constant in order to have a homogeneous medium. This simplification means that the light is isotropic in the system. The tissue was considered at 25 °C which was usually the room temperature during the trials. Along the axis the heat flux is set to 0 since in heat transfer problem with cylindrical geometry is good practice to assume this boundary condition. All the parameters such as scattering coefficient, attenuation, thermal conductivity and all the ones used were taken from a previous work of thesis.

Two different beam shapes have been tested: a rectangular window and a Gaussian. This means we had two different modelization of the heat source, with in common only the behaviour along the z-axis. The modulation on the radial direction is of course different. Different power lever were tested in agree with the *ex-vivo* tests: 0.5W, 1 W, 1.5 W, 2 W.

The best model is with the rectangular window shape since the probe used during our trials is a multi-mode optical fibre, therefor it has a more distributed power output. The reason no higher values were tested is also linked to the probe dimension: during *in-vivo* laser ablation the delivery fibre used is a single-mode, therefor the power density is higher.

The *ex-vivo* liver ablation performed have been many and we could see that temperatures measured changes with changing liver as well as for the same liver during the day, for same power values.

The trials done have been standardized during the project: three optical fibres have been used to sense temperature othogonally, along the laser axis and parallel to it 1mm further. As well as for the model the choice of power values has been 0.5, 1, 1.5 and 2 W.

After acquiring all these data it was possible to start optimization. First thing first is to obtain a vector of temperature from each power value tried during *ex-vivo* trials. This vector was used to find the values of attenuation, scattering coefficients and thermal conductivity that minimize the difference between the measured values and the ones evaluated by the model previously realized: of course in this case, the parameters to find are unknown.

Results are actually good, especially if we consider the complexity of the problem associated with all the simplifications made in order to be able to solve the problem. Even though there are differences, these helped us understand what future developments can be.

Starting from the FBGs: the optical fibres used for this work has an acrylate coating and we performed thinning when higher temperatures were reached due to the polymer melting. Using fibres with a different material may improve thermal resistance, therefor try higher power values.

Furthermore, now the model does not consider the presence of the delivery optical fibre: the medium influences the diffusion of light, as well as the heat distribution so it would be more precise and reduce the error. In the model the main problem is the heat transfer due to conduction: the further from the laser tip the temperature is calculated, the worst the match with the real measure.

The hope for the future is to be able to realize a probe that both deliver the therapy and sense the temperature distribution with the possibility of calibrating the power in relation with the measurement and the purpose. To realize a real feedback system may take a little bit more than just the work done in this thesis, but few steps have been done and with more and more this is going to be realized and will improve healthcare system as well as people recovery after surgery.

Appendix A

MATLAB Codes

A.1 Characterization

```
1 clear all
2 close all
3 clc
4 %The ultradense array is connected to channel 1, the straight array
   to channel 2.
5
6 %% Loading of the .txt file from MicronOptics
7 %to open the peaks file including the path
8 [file_p ,path_p] = uigetfile( '*.txt ', 'Load' );
9 filename_p = sprintf( '%s%s', path_p, file_p );
10 %reads the data from the peaks file into a table
11 t_p = readtable( filename_p , 'Delimiter', '\t' );
12 time_p=t_p(:,1);
13 time_array_p= table2array( time_p );
14 time_array_p = datestr( time_array_p );
15 time_p = time_array_p(:,12:end);
16 datn_p = datenum( time_p, 'HH:MM:SS' ); %convert time to string
17
18 channel = t_p(1:end-1,2:5); %number of peaks detected for
   channels
19 ch_array=table2array( channel );
20
21 peaks=t_p(1:end,6:end);
22 peaks=table2array( peaks );
23 peaks = strrep( peaks, ',', '. ' );
24 peaks_array = str2double( peaks(:, :) );
25
26 row=length( ch_array );
```

```

27 col_1 = max(ch_array(:,1));      %maximum number of detected peaks for
    channel 1
28 col_2 = max(ch_array(:,2));      %maximum number of detected peaks for
    channel 2
29
30 %CHANNEL 1
31 channel1 = peaks_array(:,1:20);
32 %CHANNEL 2
33 channel2 = peaks_array(:,21:40);
34
35 %% Plotting the signals before filtering to see the proper number of
    samples to use for averaging.
36
37 j =0;
38 if col_1~=0
39     for i=1:col_1
40         j=j+1;
41         figure (j)
42         plot(channel1(:,j),'c','LineWidth',2);
43         hold on
44         grid on
45         ax = gca; %current axes
46         ax.FontSize = 15;
47         xlabel ('Samples')
48         ylabel ('Wavelength (nm)')
49         title ( [ 'Channel 1 // Pre-filtered Wavelength, pair of FBGs
    number ' num2str(j) ] , 'fontsize',18)
50     end
51 end
52
53
54 j =0;
55 if col_2~=0
56     for i=1:col_2
57         j=j+1;
58         figure (j)
59         plot(channel2(:,j),'c','LineWidth',2);
60         hold on
61         grid on
62         ax = gca; % c u r r e n t a x e s
63         ax.FontSize = 15;
64         xlabel ('Samples')
65         ylabel ('Wavelength (nm)')
66         title ( [ 'Channel 2 // Pre-filtered Wavelength, pair of FBGs
    number ' num2str(j) ] , 'fontsize',18)
67     end
68 end
69
70 %% Filtering

```

```

71 nt = 100;
72 %the number of samples have to be the same for the MicronOptics' file
    and for the therocouple. It is the maximum number of samples that
    keeps the trend.
73
74 %filter coefficient
75 a = 1;
76 b = ones(1,nt)/nt;
77 peaks_array_f = filtfilt(b,a,peaks_array);
78 peaks_array_Nf = peaks_array (50:end-50,:);
79 datn_p2 = datn_p(50:end-50,:); %new temporal axis that match the
    filtered signal
80
81
82 % Plot of filtered and un-filtered signal overlapped.
83 j=0;
84 for i=1:col_1
85     j=j+1;
86     figure (j)
87     plot(peaks_array_Nf(:,i),'c','LineWidth',1);
88     hold on
89     plot(peaks_array_f(:,i),'m','LineWidth',2);
90     grid on
91     ax = gca; % current axes
92     ax.FontSize = 15;
93     legend('Unfiltered','Filtered')
94     xlabel('Samples')
95     ylabel('Wavelength (nm)')
96     title(['Channel 1 // Effect of filtering, FBG num ', num2str(
j) ], 'fontsize',18)
97     hold off
98 end
99
100 j=0;
101 for i=1:col_2
102     j=j+1;
103     figure (j)
104     plot(peaks_array_Nf(:,i+20),'c','LineWidth',1);
105     hold on
106     plot(peaks_array_f(:,i+20),'m','LineWidth',2);
107     grid on
108     ax = gca; % current axes
109     ax.FontSize = 15;
110     legend('Unfiltered','Filtered')
111     xlabel('Samples')
112     ylabel('Wavelength (nm)')
113     title(['Channel 2 // Effect of filtering, FBG num ', num2str(
j) ], 'fontsize',18)
114     hold off

```

```

115 end
116
117 %% THERMOCOUPLE FILE
118
119 [file_t,path_t] = uigetfile('*.log','Load');
120 filename_t = sprintf('%s%s',path_t,file_t);
121 t_t = readtable(filename_t,'FileType','text');
122 time_t = t_t(8:end,1);
123 time_array_t = table2array(time_t);
124 time_array_t = datestr(time_array_t);
125 time_array_t = time_array_t(:,12:end);
126 datn_t = datenum(time_array_t,'HH:MM:SS');
127
128 temperature = t_t(8:end,2);
129 temperature = table2array(temperature);
130 temperature = str2double(temperature);
131
132 %% Filtering thermocouple file using the same parameters used for the
    peaks.
133
134 temperature_f = filter(b,a,temperature);
135 temperature_f = temperature_f(50:end-50,:);
136 datn_t2 = datn_t(50:end-50,:);
137
138 %% Creation of a common temporal axis for thermocouple and peaks.
139 % The aim is to associate each measure of the thermocouple to the
140 % peak detected at the same instant of time.
141
142 l_max = max(length(datn_p2),length(datn_t2));
143 col = (size(peaks_array_f,2)+2);
144 data = zeros(l_max, col);
145 k = 1;
146 t=datn_t2';
147 % The matrix data has in the first column time (expressed as an array
    ), in the second the temperature at that time and the remaining
    columns are occupied by the corresponding peaks detected.
148
149 for i = t
150     if ismember(i,datn_p2')
151         loc_t = find(datn_t2==i);
152         data(k,1) = i;
153         data(k,2)= temperature_f(loc_t);
154         loc_p = find(datn_p2==i);
155         data(k,3:end)=peaks_array_f(loc_p,:);
156         k=k+1;
157     end
158 end
159
160 %% Isolating the descending temperature trend.

```

```

161 i=1;
162 while data(i,2) ~= max(data(:,2))
163     data(i,:) = [];
164 end
165
166 i=1;
167 while data(i,2) > 80.0
168     data(i,:) = [];
169 end
170
171 i=length(data);
172 while data(i,2) < 27.0
173     data(i,:) = [];
174     i=length(data);
175 end
176
177 %% Coefficients are found interpolating the data.
178 % k (the slope of the straight line) is in the first column, lambda_0
    (intercept) the second.
179
180 matr_coeff = zeros(size(data,2)-2,2);
181
182 for i = 3:size(data,2)
183     matr_coeff(i-2,:) = polyfit(data(:,2),data(:,i),1);
184 end
185
186 matr_HD = matr_coeff(1:20,:);
187 matr_straight = matr_coeff(21:end,:);
188
189 figure()
190 plot(data(:,1),data(:,2),'LineWidth',1);
191 hold on
192 datetick('x','HH:MM:SS','kepticks');
193 grid on
194 ax = gca; % c u r r e n t axes
195 ax.FontSize = 12;
196 xlabel('Absolute time')
197 ylabel('Temperature \circ C')
198 title(['Termocouple'], 'fontsize',18)
199
200
201 %% Evaluation of temperature with the coefficients
202 %the inverse formula of Bragg Wavelength is used.
203
204 col = size(peaks_array_f,2);
205
206 Temp = zeros(size(data,1),size(peaks_array_f),col);
207
208 for j = 1:col

```

```

209     Temp(:,j) = (data(:,j+2) - matr_coeff_filter(j,2))/
        matr_coeff_filter(j,1);
210 end
211
212 k=1;
213 for i = 1:20:80
214     figure(k);
215     plot(data(:,1), Temp(:,i:i+19), 'LineWidth',1);
216     hold on
217     datetick('x', 'HH:MM:SS', 'keepticks');
218     grid on
219     ax = gca; % c u r r e n t axes
220     ax.FontSize = 12;
221     xlabel('Absolute time')
222     ylabel('Temperature (^{\circ}C)')
223     k = k+1;
224 end
225
226 %% Evaluation of the quality of fitting
227
228 row = size(data,1);
229 col = size(peaks_array_f,2);
230
231 lambda_s = zeros(row, col); %experimental lambdas
232 lambda_m = data(:,3:end);
233 temperature_m = data(:,2); %measured temperature
234
235 for i = 1:col
236     lambda_s_straight(:,i) = matr_coeff(i,2) + matr_coeff(i,1)*
        temperature_m;
237 end
238
239 %Absolute error in the evaluation of temperature:
240
241 delta_t = zeros(row, col_1);
242 for i = 1:col_1
243     delta_t(:,i) = (lambda_m(:,i)-lambda_s(:,i))./ matr_coeff(i,1);
244 end
245
246
247 temperature_s = zeros(row, col); %temperature "sensed" by the FBGs
248
249 for i=1:col
250     temperature_s(:,i) = (lambda_m(:,i) - matr_coeff(i,2))./
        matr_coeff(i,1);
251 end
252
253 % Relative error:
254

```

```
255 error = zeros(row,col_);
256 for i = 1:col
257     error(:,i) = (temperature_m - temperature_straight(:,i))./
                temperature_m;
258 end
259
260 %% Plotting temperature sensed by thermocouple and the one evaluated
    using FBGs.
261
262 figure ()
263 plot(data(:,1),temperature_m,'LineWidth',2);
264 hold on
265 plot(data(:,1),temperature_s(:,1:col_1),'LineWidth',2); %HD
266 grid on
267 datetick('x','HH:MM:SS','kepticks');
268 ax = gca; %current axes
269 ax.FontSize = 15;
270 ylim([30 80])
271 xlabel('Time (s)')
272 ylabel('Wavelength (nm)')
273 title(['Comparison'], 'fontsize',18)
274 hold off
275
276 figure ()
277 plot(data(:,1),temperature_m,'b','LineWidth',2);
278 hold on
279 plot(data(:,1),temperature_s(:,col_1+1:end),'r','LineWidth',2);
280 grid on
281 ylim([30 80])
282 datetick('x','HH:MM:SS','kepticks');
283 ax = gca; %current axes
284 ax.FontSize = 15;
285 legend('Thermocouple','Evaluated')
286 xlabel('Time (s)')
287 ylabel('Wavelength (nm)')
288 title(['Comparison'], 'fontsize',18)
289 hold off
```

A.2 Thermal model code

```

1 %% RECTANGULAR BEAM MODEL
2 clearvars
3 clc
4 close all
5
6 %% Create a transient thermal model.
7 thermalmodelT = createpde('thermal','transient');
8
9 %% Include the geometry in the model.
10 r1 = [3 4 0 1e-2 1e-2 0 -0.5e-2 -0.5e-2 1e-2 1e-2];
11 gdm = [r1]';
12 %%geometry description matrix
13 ge = decsg(gdm,'R1',['R1']');
14 gm = geometryFromEdges(thermalmodelT,ge);
15
16 %% Show the model geometry
17 figure(1);
18 pdegplot(gm,'EdgeLabels','on','FaceLabels','on','VertexLabels','on')
19 axis equal
20 saveas(gcf,'geometry.png');
21
22 %% Assign thermal properties of the material to the model.
23 k = @(location,state) 0.57*location.x;
24 c = @(location,state) 3500*location.x;
25 rho = 1070;
26
27 thermalProperties(thermalmodelT,'ThermalConductivity',k,'MassDensity',
28     ...,
29     rho,'SpecificHeat',c);
30
31 %% Specify internal heat sources Q within the geometry.
32 p = 2; % Optical power (W).
33 r0=0.00005; % Fiber radius
34 u_a = 76; % Absorption coefficient (1/m)
35 u_s = 10015; % Scattering coefficient (1/m)
36 g = 0.9; % Degree of anisotropy of the scattering phase
37 function (dimentionless)
38
39 sigma_0=r0;
40 u_eff=sqrt(3*u_a*(u_a+u_s*(1-g)));
41 n=1.33; % Refractive index
42 theta=asin(0.22/n);
43 sigma=@(location,state)(sigma_0+tan(theta).*location.y);
44

```

```

43 rect=@(location ,state) ones(1,numel(location.x)).*(abs(location.x)<
    sigma(location ,state));
44
45 q = @(location ,state) alfa.(p./((pi).((sigma(location ,state)).(sigma(
    location ,state))))).*rect(location ,state).*exp(-alfa_eff.((
    location.y))).*(location.x).*heaviside(location.y);
46
47 internalHeatSource(thermalmodelT ,q);
48
49 %% Specify temperatures on the boundaries or heat fluxes through the
    boundaries
50 thermalBC(thermalmodelT , 'Edge' ,[1,2,3] , 'Temperature' ,25);
51 thermalBC(thermalmodelT , 'Edge' ,[4] , 'HeatFlux' ,0);
52
53 %% Set an initial temperature
54 T0 = 25;
55 thermalIC(thermalmodelT ,T0);
56
57 %% Mesh the geometry to the model
58 msh=generateMesh(thermalmodelT , 'Hmax' ,0.00005);
59
60 %% Show the mesh
61 figure(2);
62 pdeplot(thermalmodelT);
63 axis equal
64 title 'Block With Finite Element Mesh Displayed'
65 saveas(gcf , "mesh.png");
66
67 %% Solve
68 tlist = 0:1:180;
69 R = solve(thermalmodelT ,tlist);
70 T = R.Temperature;
71
72 %% Plot results
73 getClosestNode = @(p,x,y) min((p(1,:) - x).^2 + (p(2,:) - y).^2);
74 [~,nid1] = getClosestNode(msh.Nodes , 0 , 0.0002);
75 [~,nid2] = getClosestNode(msh.Nodes , 0 , 0.002);
76 [~,nid3] = getClosestNode(msh.Nodes , 0 , 0.004);
77 [~,nid4] = getClosestNode(msh.Nodes , 0 , 0.008);
78
79 h = figure;
80 h.Position = [1 1 2 1].*h.Position;
81
82 subplot(1,2,1);
83 pdeplot(thermalmodelT , 'XYData' ,T(:,end) , 'Contour' , 'on' , 'ColorMap' , '
    hot');
84 axis equal
85 axis equal
86 title 'Temperature , Final Time, Transient Solution'

```

```
87 |
88 | subplot(1,2,2);
89 | axis equal
90 | plot(tlist(1:size(T,2)), T(nid1,:));
91 | hold on
92 | plot(tlist(1:size(T,2)), T(nid2,:));
93 | hold on
94 | plot(tlist(1:size(T,2)), T(nid3,:));
95 | hold on
96 | plot(tlist(1:size(T,2)), T(nid4,:));
97 | grid on
98 | title 'Temperature as a Function of Time';
99 | xlabel 'Time, seconds'
100 | ylabel 'Temperature, degrees-Celsius'
101 |
102 | saveas(gcf, "results.png");
```

Bibliography

- [1] Elisabete Weiderpass Gary Reedy Cary Adams. *The Cancer Atlas. Third edition*. 250 Williams Street Atlanta, Georgia 30303 USA: American Cancer Society, Inc., 2019 (cit. on pp. 1, 2).
- [2] Sathira Kasun Perera, Susannah Jacob, Brooke E Wilson, Jacques Ferlay, Freddie Bray, Richard Sullivan, and Michael Barton. «Global demand for cancer surgery and an estimate of the optimal surgical and anaesthesia workforce between 2018 and 2040: a population-based modelling study». In: *The Lancet Oncology* (2021) (cit. on p. 2).
- [3] Cancer.Net. *What is Cancer Surgery?* <https://www.cancer.net/navigating-cancer-care/how-cancer-treated/surgery/what-cancer-surgery>, accessed 2021-01-29 (cit. on pp. 2, 5).
- [4] Chris J Diederich. «Thermal ablation and high-temperature thermal therapy: overview of technology and clinical implementation». In: *International journal of hyperthermia : the official journal of European Society for Hyperthermic Oncology, North American Hyperthermia Group* 21.8 (Dec. 2005), pp. 745–753. ISSN: 0265-6736. DOI: 10.1080/02656730500271692. URL: <https://doi.org/10.1080/02656730500271692> (cit. on pp. 5, 6).
- [5] M. Nikfarjam, V. Muralidharan, and C. Christophi. «Mechanisms of focal heat destruction of liver tumors.» In: *The Journal of surgical research* 127 2 (2005), pp. 208–23 (cit. on p. 5).
- [6] J.G. Baust, A.A. Gage, T.E. Bjerklund Johansen, and J.M. Baust. «Mechanisms of cryoablation: Clinical consequences on malignant tumors». In: *Cryobiology* 68.1 (2014), pp. 1–11. ISSN: 0011-2240. DOI: <https://doi.org/10.1016/j.cryobiol.2013.11.001>. URL: <https://www.sciencedirect.com/science/article/pii/S0011224013003969> (cit. on p. 6).
- [7] John G Baust, Andrew A Gage, Anthony T Robilotto, and John M Baust. «The pathophysiology of thermoablation: optimizing cryoablation». In: *Current Opinion in Urology* 19.2 (2009), pp. 127–132 (cit. on p. 7).

- [8] S Nahum Goldberg, G Scott Gazelle, Luigi Solbiati, William J Rittman, and Peter R Mueller. «Radiofrequency tissue ablation: increased lesion diameter with a perfusion electrode». In: *Academic radiology* 3.8 (1996), pp. 636–644 (cit. on p. 7).
- [9] Al B Barqawi and E David Crawford. «Emerging role of HIFU as a noninvasive ablative method to treat localized prostate cancer». In: *Oncology* 22.2 (2008), p. 123 (cit. on p. 8).
- [10] Christopher Rowland Hill, Jeff C Bamber, and Gail R ter Haar. *Physical principles of medical ultrasonics*. 2004 (cit. on p. 8).
- [11] Dr >Gail ter Haar and Constantin Coussios. «High intensity focused ultrasound: Physical principles and devices». In: *International Journal of Hyperthermia* 23.2 (2007). PMID: 17578335, pp. 89–104. DOI: 10.1080/02656730601186138. eprint: <https://doi.org/10.1080/02656730601186138>. URL: <https://doi.org/10.1080/02656730601186138> (cit. on p. 9).
- [12] *Radiofrequency Ablation*. <https://www.asiancancer.com/cancer-therapies/radiofrequency-ablation/> (cit. on p. 9).
- [13] Emiliano Schena, Paola Saccomandi, and Yuman Fong. «Laser Ablation for Cancer: Past, Present and Future». In: *Journal of Functional Biomaterials* 8.2 (2017). ISSN: 2079-4983. DOI: 10.3390/jfb8020019. URL: <https://www.mdpi.com/2079-4983/8/2/19> (cit. on p. 9).
- [14] M. Cutroneo, Lorenzo Torrisi, and Cristina Scolaro. «Laser applications in bio-medical field». In: 2010 (July 2012) (cit. on p. 10).
- [15] *Laser*. <https://it.wikipedia.org/wiki/Laser> (cit. on p. 12).
- [16] <http://dataland-network.com/2016/05/02/8-advantages-of-choosing-fiber/> (cit. on p. 13).
- [17] <https://line.17qq.com/articles/odngcmcov.html> (cit. on p. 14).
- [18] PhD Valter Kiisk. *Principles of Raman spectroscopy* (cit. on p. 16).
- [19] Steven L Jacques. «Optical properties of biological tissues: a review». In: *Physics in Medicine & Biology* 58.11 (2013), R37 (cit. on p. 17).
- [20] Alfred Vogel and Vasan Venugopalan. «Mechanisms of Pulsed Laser Ablation of Biological Tissues». In: *Chemical Reviews* 103.2 (2003), pp. 577–644 (cit. on p. 16).
- [21] M. Cutroneo, Lorenzo Torrisi, and Cristina Scolaro. «Laser applications in bio-medical field». In: 2010 (July 2012) (cit. on p. 17).
- [22] M. J. C. van Gemert and A. J. Welch. «Clinical use of laser-tissue interactions». In: *IEEE Engineering in Medicine and Biology Magazine* 8.4 (1989), pp. 10–13. DOI: 10.1109/51.45950 (cit. on p. 18).

- [23] Edoardo Puleo. «Sviluppo di un sistema di Ablazione Laser in ambiente oncologico = Development of a system for Laser Ablation in oncology». Mar. 2020. URL: <http://webthesis.biblio.polito.it/13761/> (cit. on p. 19).
- [24] Michael Bakaic, Matthew Hanna, Cyril Hnatovsky, Dan Grobnic, Stephen Mihailov, S Stefan Zeisler, and Cornelia Hoehr. «Fiber-Optic Bragg Gratings for Temperature and Pressure Measurements in Isotope Production Targets for Nuclear Medicine». In: *Applied Sciences* 10.13 (2020), p. 4610 (cit. on p. 20).
- [25] Guido Perrone Daniele Tosi. *Fiber-Optic Sensors for Biomedical Applications*. Artech House, 2017 (cit. on p. 22).
- [26] Ing. Jaroslav TÝNEK. «MANUFACTURING OF THE FIBER BRAGG GRATINGS». In: (), p. 5 (cit. on pp. 22, 24).
- [27] *Fiber Bragg grating*. URL: https://en.wikipedia.org/wiki/Fiber_Bragg_grating (cit. on p. 26).
- [28] Hong-Hu Zhu, Bin Shi, and Cheng-Cheng Zhang. «FBG-Based Monitoring of Geohazards: Current Status and Trends». In: *Sensors* 17.3 (2017). ISSN: 1424-8220. DOI: 10.3390/s17030452. URL: <https://www.mdpi.com/1424-8220/17/3/452> (cit. on p. 27).
- [29] *Heat Transfer*. <https://it.mathworks.com/help/pde/heat-transfer-and-diffusion-equations.html> (cit. on p. 50).
- [30] Akira Ishimaru. «Diffusion of light in turbid material». In: *Appl. Opt.* 28.12 (June 1989), pp. 2210–2215. DOI: 10.1364/AO.28.002210. URL: <http://ao.osa.org/abstract.cfm?URI=ao-28-12-2210> (cit. on p. 53).
- [31] Alessandra Beccaria. «Studio teorico e sperimentale del comportamento termo-ottico di tessuti biologici per il trattamento di tumori mediante ablazione laser = Theoretical and experimental study of thermo-optical behaviour of biological tissues for tumours treatment with laser ablation». Oct. 2019. URL: <http://webthesis.biblio.polito.it/12255/> (cit. on p. 53).
- [32] Paola Saccomandi, Emiliano Schena, M. Caponero, Francesco Di Matteo, Margaret Martino, Monica Pandolfi, and Sergio Silvestri. «Theoretical Analysis and Experimental Evaluation of Laser-Induced Interstitial Thermotherapy in Ex Vivo Porcine Pancreas». In: *IEEE transactions on bio-medical engineering* 59 (Aug. 2012), pp. 2958–64. DOI: 10.1109/TBME.2012.2210895 (cit. on p. 54).
- [33] Giuseppe Poma. «Laser medicali per ablazione di tumori = Medical lasers for tumors ablation». Dec. 2020. URL: <http://webthesis.biblio.polito.it/16973/> (cit. on p. 61).